Finite Theory: Revisiting the Variable-Speed-of-Light Model of Gravitation, with Exploratory Bench Tests

Phil Bouchard CEO & Founder

Fornux Inc.
3909 S Maryland Pkwy Ste 314, #638,
Las Vegas, 89119, NV, United States.

Contributing authors: phil@fornux.com;

Abstract

A gravitational model is proposed in which the speed of light, and with it the time rate, varies with the superimposed gravitational potentials. With the speed of light postulated as the square of the time rate, and an adopted orbital law, the model reproduces the bending and delay of light and, to leading order, the perihelion precession, matching General Relativity to first order. It fits galactic rotation curves with three parameters per curve, without dark matter but without excluding it.

Gravitoelectromagnetism (GEM) is employed at the macroscopic level to formulate these relations. By conceptualizing both electromagnetic and gravitoelectromagnetic fields as energy distributions, a force is proposed as the derivative of an interaction energy, an additional hypothesis.

Six preliminary bench investigations are reported. Under the adopted steel-reference calibration, paired free-fall drops give an apparent lower-half acceleration deficit of the NdFeB sphere of about 21 %, which unresolved calibration-transfer effects prevent identifying as a physical anomaly. Two pendulum configurations differ in period by 0.8 %; estimated corrections leave 0.47 to 0.53 %, whose reading as a mass-ratio difference is conditional on the effective-length and restoring-force model. A floating magnet drifts in a direction that changes between runs, and one weighed on either face differs by 0.1 g, both unexplained; a spinning disc on a balance gives speed-dependent load changes within range and calibration limitations; and a liquid-gallium vortex run was inconclusive. None of these measurements validates the proposed mechanism.

Each relation of this conjectural model is labelled as postulated, imported, derived, fitted or conjectured.

Keywords: Perihelion Shift, Light Bending, Rotation Curve, Variable Speed of Light, Gravitoelectromagnetism, Free Fall

1 Introduction

This is a reevaluation of A. Einstein's initial proposal to use the Variable Speed of Light (VSL) in 1911, which was subsequently extended by R. Dicke in 1957 [16]. In this work, we extract alternative interpretations, apply corrections, and introduce new fundamental hypotheses, resulting in a new gravitational model. Reported observations of speed-of-light anisotropies (see: [12] and [23]) motivate it. An open-source simulator integrates bodies under the time-dilation factor of the theory, with scenes ranging from atoms to the solar system and a galactic bulge [10].

The Finite Theory presented herein is a conjecture built on the definitions and hypotheses of Sec. 2.1; Table 1 labels each relation used as a postulate, an imported result, a parameter, a derived consequence, a fit or a conjecture. As a further conjecture, by considering both gravity (as monopole gravitoelectric field) and time rate (as an induced monopole gravitomagnetic field) as fundamental virtual particles, it may be possible to manipulate and control them.

2 Foundation of the Finite Theory

2.1 Hypotheses of the Finite Theory

Finite Theory introduces a novel representation of the formulas derived from General Relativity that is based on the time dilation induced by the energy density, of any form (EM and GEM).

In contrast to General Relativity, where space-time is represented using non-Euclidean geometry to maintain the constancy of the speed-of-light while allowing space to vary, Finite Theory posits that the speed-of-light (and therefore the time rate) is a positive variable within a constant space.

Hypotheses of the Finite Theory are as follows:

Definition 1 A 'comoving framework' moves coherently with the source of the strongest neighboring gravitational acceleration amplitude ($G \times m/r^2$). This means if the observer and the observed object are nearby a planet then the comoving framework is set on the planet's center, rotating with the same angular speed. Note that this can be a non-inertial frame. For example, the moons, the planets, the stars, the galaxy bulges, and the black holes all have their own comoving or rotating framework. This way there can be no absolute framework in the entire universe as they're all relative in angular velocity and gravitational acceleration amplitude to each other.

Definition 2 A 'parent framework' is the source of the 2nd strongest gravitational acceleration amplitude; the source here is a collective noun and represents the conglomeration of its constituents.

Definition 3 An 'absolute framework' is a comoving framework that has no parent framework. It is used only in the thought experiment of Sec. 4.3.1, a universe holding a single black hole.
Definition 4 Contrary to the currently accepted theory, Finite Theory proposes a radical view of gravitational time dilation, namely, is directly proportional to the ratio of the superimposed gravitational potentials of the observer and the observed object. The potentials include the background of Sec. 2.5.3, so that the ratio tends to 1 when the sources vanish. Clock comparisons are rate ratios, defined once in Sec. 2.5.4, where a second-order term is added to this ratio.
Hypothesis 1 The speed-of-light in free space has value c for any observer at rest relative to the comoving framework. However, observers in relative motion with respect to this frame will not measure the same value for c.
Hypothesis 2 The time rate of an object moving with respect to an observer at rest relative to the comoving framework is the ratio of the object's rest energy to its total energy, the rest energy plus the kinetic energy, $K = E - mc^2$, where E is the measured energy of the object and v its speed with respect to that observer; for $v \ll c$ it is $mv^2/2$.
Hypothesis 3 Any spatial variation of an energy distribution, GEM or EM, is a force, $F = -dU/dx$ [29].
Hypothesis 4 There is a distinct mass / charge equivalence.
Hypothesis 5 In the time rate of a static clock, the gravitational potential energy of the clock adds to its rest energy, and an energy of the same magnitude, the kinetic energy $m\,(dr/d\tau)^2/2 = GmS$ of a fall from rest at infinity to the place of the clock in the orbital law of Sec. 2.7, adds at right angles to their sum; the time rate is the ratio of the rest energy to the resultant (Sec. 2.5.4). This hypothesis was formulated after the form of the clock law was fixed, and it concerns static clocks and the gravitational potential only: the time rate of a moving clock remains that of Hypothesis 2.

Table 1 gives the status of the relations used in this paper. The model is local and limited: it gives clock rates, the speed of light and orbital corrections in the field of the dominant source, the comoving framework of Definition 1. It does not supply field equations, transformation rules between frameworks, or the behaviour of a clock where the dominant source changes, and its gravitoelectric and gravitomagnetic components, λ_g and μ_g, are linear mass densities, not the fields of standard gravitoelectromagnetism [21]. Below, we'll consider the consequences of these hypotheses on the time dilation effect.

2.2 Side by side comparison

Here we will study the gravitomagnetic component (μ_g) and the gravitoelectric component (λ_g) respectively, both affecting the trajectory of light and bodies in our universe.

2.2.1 Gravitomagnetic component

Given from the gravitational time dilation of General Relativity:

Table 1 Status of the relations used in this paper: postulated (definitions and hypotheses), imported from established physics, set as a parameter, derived here, fitted to data, or conjectured

Status	Relations
Postulate	Definitions 1 to 4 and Hypotheses 1 to 5 (Sec. 2.1); the clock law (38), from Definition 4, its second-order term adopted and read by Hypothesis 5 (Sec. 2.5.4), with the clock comparison (40), (41); the kinematic time rate (33), from Hypothesis 2; the second factor of the light speed (43), attributed to the energy density, with the scaling of matter that accompanies it (Sec. 2.6); the orbital law of Sec. 2.7, (54) with the angular law $d\varphi/ds = h/r^2$
Imported	Newtonian orbital energy (50), (51); relativistic momentum and energy (36), (37); the results of General Relativity quoted for comparison, (39) and Sec. 2.8.1; the measured deflection (48) and delay of light
Parameter	$\lambda_g = c^2/G$ in the solar system (11), adopted so that the clock law has the weak-field expansion of General Relativity, and $G = c^2/\lambda_g$ (15); μ_g, the background of the time rate, calibrated on the measured solar deflection discrepancy (7), which makes it equal to λ_g in the solar system
Derived	the weak-field expansions (3) to (14); the checks of the clock comparison with the sphere source (42); the refractive index (44), the ray law (45), the deflection of light (46), (47) and (49), and its delay, from the light speed (43); the perihelion shift (57), within the orbital law, through (55) and (56), and the agreement of that law, to first order, with the line element of the clock law and the light speed (Sec. 2.7); the cancellation altitude of Sec. 2.8.2; the Doppler and redshift relations of Sec. 2.10
Fit	the galactic rotation curves (91), with λ_g, m and the rotation ω of the comoving framework of each galaxy adjusted to it (Sec. 4.3.1), and μ_g for the Milky Way (Sec. 4.3.1)
Conjecture	the latitude dependence of G (81); the interaction energy and force (84) of Sec. 3, an additional hypothesis; the cosmological implications of Sec. 4, including the acceleration of the universe (93) and the position of the universal core (99)

$$t_o = \frac{\sqrt{1 - \frac{2Gm}{\|i\|c^2}}}{\sqrt{1 - \frac{2Gm}{(x+\|i\|)c^2}}} \times t_f \tag{1}$$

And from the gravitational time dilation:

$$t_o = \frac{\frac{m}{\|x-i\|} + \mu_g}{\frac{m}{\|i\|} + \mu_g} \times t_f \tag{2}$$

If we equate the aforementioned equations by using a reference point infinitely far away and letting μ_g include the properties of the galaxy. This component represents the missing observation in half of the light bending angle and the perihelion precession disparity.

$$\left(\frac{\frac{m}{r} + \mu_g}{\mu_g}\right)^{-1} \approx \frac{\sqrt{1 - \frac{2Gm}{rc^2}}}{1} \tag{3}$$

$$\left(1 + \frac{m}{r\mu_g}\right)^{-1} \approx 1 - \frac{Gm}{rc^2} \tag{4}$$

$$\left(1+\frac{m}{r\mu_g}\right)^{-2} \approx 1-\frac{2Gm}{rc^2} \tag{5}$$

For the relation to be consistent, μ_g must be defined as the following, based on the discrepancy of the observed light bending grazing the Sun:

$$\mu_g = \frac{m_s \int_{-\infty}^{\infty} \frac{r_s}{(x^2+{r_s}^2)^{\frac{3}{2}}} dx}{\delta} \tag{6}$$

$$\mu_g = \frac{2m_s}{\delta r_s} = 1.35 \times 10^{27}\, kg\, m^{-1} \tag{7}$$

Where:

- $m_s = 1.98892 \times 10^{30}\, kg$ (mass of the Sun)
- $r_s = 6.957 \times 10^{8}\, m$ (radius of the Sun)
- $\delta = 4.25 \times 10^{-6}\, rad$ (observed deflection angle discrepancy)

For the solar system μ_g therefore equals c^2/G, the gravitoelectric constant of the next subsection. For the Milky Way, the fit of (91) to its rotation curve gives $\mu_g = 4.1 \times 10^{21}\, kg\, m^{-1}$ (Sec. 4.3.1). No rule relating μ_g to the angular velocity of a galaxy is derived here; only these values are used.

Furthermore, the gravitational potential will be explained in Sec. 2.9.

2.2.2 Gravitoelectric component

A similar set of identities to the previous subsection can be applied to get a simpler fudge factor λ_g similar to μ_g. This component actually represents the gravitational acceleration used to give half of the observed perihelion precession disparity.

$$\left(\frac{\frac{m}{r}+\lambda_g}{\lambda_g}\right)^{-1} \approx \frac{\sqrt{1-\frac{2Gm}{rc^2}}}{1} \tag{8}$$

$$\left(1+\frac{m}{r\lambda_g}\right)^{-1} \approx 1-\frac{Gm}{rc^2} \tag{9}$$

$$\left(1+\frac{m}{r\lambda_g}\right)^{-2} \approx 1-\frac{2Gm}{rc^2} \tag{10}$$

In this case for the relation to be consistent, λ_g must be defined as:

$$\lambda_g = \frac{c^2}{G} = 1.35 \times 10^{27}\, kg\, m^{-1} \tag{11}$$

Therefore, λ_g is simply the Planck linear mass density. Given the observed deflection angle is exactly twice the Newtonian value $2Gm_s/(c^2 r_s)$, the calibration (7) makes both components equal:

$$\left(\frac{\frac{m_s}{r_s}+\mu_g}{\mu_g}\right)^{-1} = \left(\frac{\frac{m_s}{r_s}+\lambda_g}{\lambda_g}\right)^{-1} \tag{12}$$

$$\left(1+\frac{m_s}{r_s\mu_g}\right)^{-1}=\left(1+\frac{m_s}{r_s\lambda_g}\right)^{-1} \tag{13}$$

$$\left(1+\frac{m_s}{r_s\mu_g}\right)^{-2}=\left(1+\frac{m_s}{r_s\lambda_g}\right)^{-2} \tag{14}$$

Given the aforementioned identities, we can actually easily solve Newton's gravitational variable using Equ. (11) and (13), variant for each solar system actually:

$$G=\frac{c^2}{\lambda_g} \tag{15}$$

Furthermore, integrating Equ. (7) will result in a more applicable form:

$$G=\frac{\delta c^2\, r_s}{2m_s} \tag{16}$$

The two parameters therefore have different roles and statuses. μ_g, the background of the time rate (Sec. 2.2.1), is calibrated on the measured solar deflection discrepancy δ through (7). λ_g, which sets the Newtonian acceleration through $G = c^2/\lambda_g$, is adopted as c^2/G in the solar system, so that the clock-rate form (8) has the weak-field expansion of General Relativity. The calibration makes the two equal in the solar system, and from Sec. 2.5.3 on the background of the time rate is written λ_g; this equality is the calibration, not a derivation that the two play the same physical role. In galaxies, the parameter of (91) is fitted to each rotation curve (Sec. 4.3.1). The model does not predict these values before these choices.

2.3 Kinetic time dilation factor

From Definition 1, a clock located between two comoving frameworks belongs to the one that dominates its gravitational acceleration. Between the Earth and the Sun, the share of the Earth in the gravitational acceleration at altitude x is:

$$y=\frac{\frac{m_e}{(x-p_e)^2}}{\frac{m_s}{(p_s-x)^2}+\frac{m_e}{(x-p_e)^2}} \tag{17}$$

as shown in Fig. 1.
Where:

- $p_e = -6.371\times10^6\,m$ (position of the center of the Earth)
- $m_e = 5.973\times10^{24}\,kg$ (mass of the Earth)
- $p_s = 1.49598\times10^{11}\,m$ (position of the center of the Sun)
- $m_s = 1.98892\times10^{30}\,kg$ (mass of the Sun)

At the altitude of the GPS satellites, $20\,200\,km$, $y = 0.990$: the Earth provides 99 % of the gravitational acceleration, so it is the comoving framework of the satellites and their kinetic time dilation is the one relative to the Earth (Sec. 2.8.2). The Earth and the Sun contribute equally ($y = 1/2$) at $2.59\times10^8\,m$ from the center of the Earth; beyond that distance the Sun is the comoving framework.

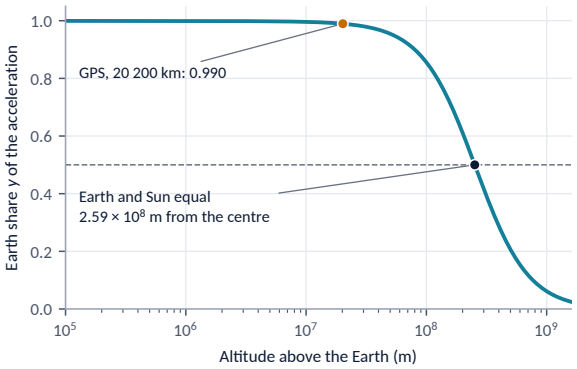

Fig. 1 Share of the Earth in the gravitational acceleration between the Earth and the Sun

The kinetic time dilation is not shared between the two frameworks in proportion to y. A share of $1 - y = 1.0\,\%$ relative to the Sun, about which the satellites move at $30\,km/s$, would make the GPS satellite clocks gain $34.3\,\mu s$ per day instead of $38.5\,\mu s$ per day, against the offset of $38.6\,\mu s$ per day built into them [2].

2.4 Gravitational time contraction

Since in the candidate theory, the acceleration is defined by gravitons pulling the body in the opposite direction of their velocity, the net effect of the gravitational acceleration already defines the flux. Unlike kinetic time dilation this is not an incident event but the residuum of the modus operandi by the acceleration vector magnitude.

In contrast to kinetic time dilation, gravitational time contraction will be used interdependently with the non-trivial ambient gravity field of the observer or rationalized.

2.4.1 Inverse square law 1

Given that FT gravitational time dilation and the Newtonian gravity force are similar, the standard model of gravity inside a sphere cannot be directly linked with FT because factors applied in one direction will not cancel their equivalent in the opposite direction. This means no simplification can be made and all infinitesimal elements of the mass will affect the net amplitude at one particular location. The factor f below is therefore a scalar: it adds the magnitudes $1/r^2$ of the contributions of all mass elements without their directions. It is not the vector gravitational acceleration, whose contributions cancel by symmetry, for instance at the centre of the sphere. First, we can represent the respective factor with a triple integral in the following way, using spherical coordinates:

$$f = \frac{2\pi \int_0^r \rho^2 d\rho \int_0^\pi \sin(\theta) d\theta}{r^2} \tag{18}$$

Given:

$$r^2 = (\cos(\theta)r_1 - z_2)^2 + (\sin(\Phi)\sin(\theta)r_1 - y_2)^2 + (\cos(\Phi)\sin(\theta)r_1 - x_2)^2 \tag{19}$$

After simplification:

$$f = \frac{2\pi \int_0^r \rho^2 d\rho \int_0^\pi \sin(\theta) d\theta}{-2\rho d_2 \cos\theta + d_2^2 + \rho^2} \tag{20}$$

Namely:

$$f = -\frac{\pi\left(2\left({d_2}^2 - {r_1}^2\right)\log(r_1 + d_2) + 2\log|d_2 - r_1|\left({r_1}^2 - {d_2}^2\right) - 4d_2 r_1\right)}{2d_2} \tag{21}$$

Where:

- r_1 is the spherical mass radius
- d_2 is the distance of the observer from the center

2.4.2 Inverse square law 2

Different means of calculating the inner gravitational time dilation factor with no relation to the aforementioned procedure can also be used. It consists of calculating the intersection between a growing sphere held within the spherical body in question.

This is done by first calculating all sphere surfaces fitting inside the largest sphere not in intersection with the spherical body.

Now for the second part, the spherical cap surface area resulting from the intersection of the two spheres will have to be considered only.

By summing up both areas we will have:

$$f = \int_{r_1 - d_2}^{r_1 + d_2} \frac{2\pi r_2 \left(\frac{d_2^2 - r_2^2 + r_1^2}{2d_2} + r_2 - d_2\right)}{r_2^2} \mathrm{d}r_2 + \int_0^{r_1 - d_2} \frac{4\pi r_2^2}{r_2^2} \mathrm{d}r_2 \tag{22}$$

$$f = \frac{\pi\left[d_2^2 \log\left(\frac{r_1 + d_2}{r_1 - d_2}\right) + r_1^2 \log\left(\frac{r_1 - d_2}{r_1 + d_2}\right) + 2d_2 r_1 - 4d_2^2\right]}{-d_2} + 4\pi(r_1 - d_2) \tag{23}$$

Where:

- r_1 is the spherical mass radius
- d_2 is the distance of the observer from the center

Both of the previous method will result in the following inside and outside the sphere scalar gravitational acceleration factor as seen in Fig 2.

2.4.3 Inside a sphere

By putting Equation (23) into the context of the gravitational potential, we will have to reduce the degree of the inverse radius down to 1:

$$f = \int_{r_1-d_2}^{r_1+d_2} \frac{2\pi r_2 \left(\frac{d_2^2-r_2^2+r_1^2}{2d_2} + r_2 - d_2\right)}{r_2} \mathrm{d}r_2 + \int_0^{r_1-d_2} \frac{4\pi r_2^2}{r_2} \mathrm{d}r_2 \tag{24}$$

$$f = \frac{4\pi d_2 \left(3r_1 - 2d_2\right)}{3} + 2\pi \left(r_1 - d_2\right)^2 \tag{25}$$

Where:

- r_1 is the spherical mass radius
- d_2 is the distance of the clock from the center

Or more generically for a clock at a specific position inside one spherical mass, as seen from an observer positioned in a null environment:

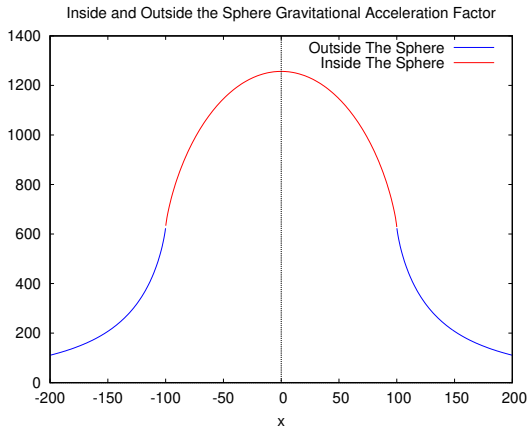

Fig. 2 Inside and Outside the Sphere Scalar Gravitational Acceleration Factor

$$Q = \frac{S\left(r\right)}{S\left(r_o\right)} \tag{26}$$

$$Q = \frac{2\pi \left(3r_s^2 - r^2\right) 3\rho}{2\pi \left(3r_s^2 - r_o^2\right) 3\rho} \tag{27}$$

$$Q = \frac{3r_s^2 - r^2}{3r_s^2 - r_o^2} \tag{28}$$

Where:

- r is the location of the clock
- r_s is the radius of the spherical mass
- r_o is the location of the observer

This source ratio Q, like the one of the next subsection, compares the source terms S only; it is a dimensionless intermediate quantity, not an observable clock comparison: it does not depend on the density of the sphere and so does not tend to 1 as the

density tends to zero. The observable comparison is (41) of Sec. 2.5.4, which adds the background; it tends to 1 when the source vanishes, equals 1 for coincident clocks, and is continuous at the surface of the sphere.

2.4.4 Outside a sphere

We can now estimate the amplitude of the gravitational potential by sampling anchored bodies at an infinitesimal position by consequently rationalizing the measurement with the amplitude derived from the location of the observer.

Since an inertial body being subject to a specific gravitational force is responsible for gravitational time dilation and gravity is a superposable force, we will translate the same conditions of all gravitational potentials into the sum of all surrounding fields of an observed clock and the observer:

$$Q = \frac{S(r)}{S(r_o)} \tag{29}$$

$$Q = \frac{\sum_{i=1}^{n} \frac{m_i}{\|r_i - r\|}}{\sum_{i=1}^{n} \frac{m_i}{\|r_i - r_o\|}} \tag{30}$$

Where:

- r is the location of the observed clock
- r_i is the location of the center of mass i
- r_o is the location of the observer (typically $0m$)
- m_i is the mass i
- Q is the source ratio, a dimensionless intermediate quantity; the observable comparison is (41)

2.4.5 Inside and Outside a sphere

Let's integrate the 2 forms with the following example where we'll use the following properties:

- $\lambda_g = \frac{c^2}{G}$
- $\lambda_u = \lambda_g \times c^2$
- $\lambda_{eg} = \sqrt{\frac{K}{G}}$

And apply them using the inside the sphere gravitational potentials for $x < r_s$:

$$t_o = \lim_{s \to \infty} \frac{\frac{q_s \lambda_{eg} c^2}{s} + \lambda_u}{\frac{q_s \lambda_{eg} c^2 (3{r_s}^2 - x^2)}{2{r_s}^3} + \lambda_u} \times t_f \tag{31}$$

And the outside the sphere gravitational potentials to determine the effective time dilation factor for $x > r_s$:

$$t_o = \lim_{s \to \infty} \frac{\frac{q_s \lambda_{eg} c^2}{s} + \lambda_u}{\frac{q_s \lambda_{eg} c^2}{x} + \lambda_u} \times t_f \tag{32}$$

Where:

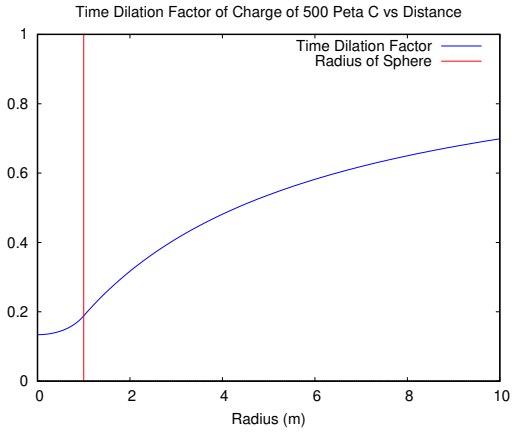

Fig. 3 Inside and Outside the Sphere Gravitational Potential Factor

- s is the position of the observer
- q_s is the charge of the sphere
- r_s is the radius of the spherical charge

2.5 Time dilation effect

2.5.1 Kinematic time dilation

Following Hypothesis 2, the time rate of a moving object is the ratio of its rest energy to its total energy, the same kind of energy ratio that sets the gravitational time rate (Definition 4):

$$\frac{\Delta\tau_v}{\Delta\tau_0} = \frac{m_0c^2}{m_0c^2 + K} \tag{33}$$

Here, $\Delta\tau_v$ is the interval of time between some events measured in the proper reference of the moving observer and $\Delta\tau_0$ is an interval of time between the same events measured by the static observer. m_0 and K are the rest mass and the kinetic energy of the moving observer, v is its velocity measured by the static observer and $c = 2.998 \times 10^8\, m/s$ is the speed-of-light.

For $v \ll c$ the kinetic energy is the classical $K = m_0v^2/2$ (Hypothesis 2), and to first order in v^2/c^2:

$$\frac{\Delta\tau_v}{\Delta\tau_0} = \frac{1}{1 + \frac{v^2}{2c^2}} \approx 1 - \frac{v^2}{2c^2} \tag{34}$$

The kinematic shift of the time rate is therefore the kinetic energy per unit rest energy, $K/(m_0c^2)$, in the same way as the gravitational shift is the potential energy per unit rest energy, $Gm/(c^2r)$.

At higher speeds the kinetic energy is $E - m_0c^2$ (Hypothesis 2). Bertozzi measured the speed and the kinetic energy of accelerated electrons independently and found $E = m_0c^2/\sqrt{1 - v^2/c^2}$ [4]. With this energy, (33) becomes

$$\frac{\Delta\tau_v}{\Delta\tau_0} = \sqrt{1 - \frac{v^2}{c^2}} \tag{35}$$

which coincides with the special relativistic result and reduces to (34) for $v \ll c$. It is confirmed directly by muons circulating in a storage ring at $\gamma = 29.33$: their measured lifetime of $64.4\,\mu s$ agrees with $\gamma\tau_0 = 29.33 \times 2.197\,\mu s$ to about 0.1 % [3]. As shown in Sec. 2.8.2, combined with the gravitational effect it also gives the time dilation cancellation altitude and the clock rate observed for GPS satellites.

2.5.2 The momentum and energy of accelerated particles

With (35), the momentum and the energy of an accelerated particle are

$$p = \frac{m_0\, v}{\sqrt{1 - \frac{v^2}{c^2}}} \tag{36}$$

$$E = c\sqrt{p^2 + c^2 m_0^2} = \frac{m_0 c^2}{\sqrt{1 - \frac{v^2}{c^2}}} \tag{37}$$

The rest mass m_0 does not change with speed; what increases is the energy and the momentum of the particle.

2.5.3 Gravitational time dilation

As previously stated in Section 2.2.1, the effect of the time dilation in the gravitational field is described by the relation:

$$\frac{\Delta\tau}{\Delta t} = \frac{\lambda_g}{\sqrt{\left(\lambda_g + \frac{M}{r}\right)^2 + \left(\frac{M}{r}\right)^2}} \approx \left(1 + \frac{M}{\lambda_g r}\right)^{-1} \tag{38}$$

where, M is the mass of the gravitating object and r is the distance from its center. Under $\Delta\tau$ we mean the interval of local time at the point situated at distance r from the center of the source of gravitation. Δt is the interval of time measured by the distant observer, situated at distance $r \to \infty$. With the observer placed at infinity, the potential ratio of Sec. 2.2.1 reduces to the ratio on the right, the form of this law to first order in $M/(\lambda_g r)$, its background μ_g being written λ_g (Sec. 2.2.2), and with no source ($M \to 0$) both give a time rate of 1. The term $(M/r)^2$ under the root sets the second order of the law; it is adopted (Sec. 2.5.4).

With $\lambda_g = c^2/G$, (38) agrees to first order in $GM/(c^2 r)$ with the general relativistic time dilation, where c is the speed-of-light and $G = 6.674 \times 10^{-11}\, m^3 kg^{-1} s^{-2}$ is the gravitational constant. Indeed, we know that in the weak field limit of General Relativity, the time dilation effect in the gravitational field takes the following form (see, for example, [13]):

$$\frac{\Delta\tau}{\Delta t} = \sqrt{1 - \frac{2GM}{c^2 r}} \approx 1 - \frac{GM}{c^2 r} \tag{39}$$

To second order, with $u = GM/(c^2 r)$, (38) gives $1 - u + u^2/2$. General Relativity gives $1-u-u^2/2$ with the radial coordinate of (39) and $1-u+u^2/2$ with the isotropic radial coordinate, in which, as in the model (Sec. 2.6), the speed of light is the same in all directions: so compared, the two agree to second order and differ at the third, $+u^3/2$ against $-u^3/4$.

But due to the hypotheses of the Finite Theory, factor λ_g in (38) is not a universal constant but depends on the superimposed gravitational potentials. For example, in solar system experiments, where the gravitational potential of the Sun is the source of the strongest gravitational acceleration, we take $\lambda_g = c^2/G$ (11). This value is consistent with the deflection angle of light in the gravitational field of the Sun, as shown in the next subsection.

2.5.4 Clock comparison

One comparison is used throughout. For static clocks, let $S(r) = \sum_i m_i / \|r_i - r\|$ be the source term at the position r of a clock, in kg/m, and λ the positive background of the local domain, $\lambda = \lambda_g$ in the solar system. The rate of a static clock with respect to the distant coordinate time t is

$$R(r) = \frac{d\tau(r)}{dt} = \frac{\lambda}{\sqrt{(\lambda + S(r))^2 + S(r)^2}}, \tag{40}$$

and two static clocks at r and r_o, read over the same interval of t, compare as

$$\frac{d\tau(r)}{d\tau(r_o)} = \frac{R(r)}{R(r_o)} = \sqrt{\frac{(\lambda + S(r_o))^2 + S(r_o)^2}{(\lambda + S(r))^2 + S(r)^2}} \approx \frac{\lambda + S(r_o)}{\lambda + S(r)}. \tag{41}$$

This is a ratio of rates: the clock with the larger source term accumulates less proper time. The duration of one tick is its reciprocal and is not used. In this notation (38) is $R(r)$ for a single source, $\Delta\tau$ being read by the clock at r and Δt by the distant clock. In the potential ratio of Sec. 2.2.1 and in Sec. 2.4.5, t_o is read by the observed clock and t_f by the observer's clock over the same interval, so that $t_o/t_f = d\tau(r)/d\tau(r_o)$. The source ratios Q of Secs. 2.4.3 and 2.4.4 are intermediate quantities, not clock comparisons.

To first order in S/λ the rate (40) is the ratio $\lambda/(\lambda + S)$, and the comparison (41) the ratio on its right. The relations of Secs. 2.2.1, 2.2.2, 2.4.5, 2.8 to 2.10 and 4.1 are written with these ratios, the first-order form: in the solar system S/λ is at most 2×10^{-6}, its value at the surface of the Sun, and the second-order terms are below 10^{-11}. The term S^2 under the root is the second-order term. It is adopted, not derived: with it $R^2 = 1 - 2u + 2u^2 + \ldots$, $u = S/\lambda$, which the motion of the planets requires when the clock law and the light speed of Sec. 2.6 are read together as a line element (Sec. 2.7); the ratio alone, the clock law of the first published version, gives $1-2u+3u^2$. Any rate with the same expansion to second order meets this requirement, the exponential $e^{-S/\lambda}$ among them. The form (40) was chosen among them after the

fits of Sec. 4.3.1, where S/λ is not small, because it keeps the decrease of the ratio as λ/S at large S/λ.

Hypothesis 5 reads this form in terms of energy. For a clock of mass m, with $G = c^2/\lambda$, the ratio S/λ is the magnitude of its gravitational potential energy, GmS, per unit of its rest energy mc^2; it is also the kinetic energy, per unit rest energy, of a body that has fallen from rest at infinity to the same place, since in the orbital law (52), whose Newtonian term is exact, that body gains the kinetic energy $m\,(dr/d\tau)^2/2 = GmS$. Then

$$\frac{1}{R^2} = \left(1 + \frac{S}{\lambda}\right)^2 + \left(\frac{S}{\lambda}\right)^2$$

is the square of the rest energy increased by the potential energy, plus the square of that kinetic energy, the two being added at right angles; the two source terms are equal because the fall conserves energy. To first order this is the ratio of the rest energy to the rest energy plus the kinetic energy of the fall, the form of Hypothesis 2. The kinetic energy is that of the fall and not of the clock, which is static; a moving clock has in addition the kinematic rate (33). The hypothesis was formulated after the form (40) was chosen and is not an independent derivation of it: it replaces an adopted term by an adopted rule. Adding the momentum of the fall at right angles, as for a moving particle (36), (37), would give $1/R^2 = 1 + 4u + 2u^2$ and twice the measured redshift, so that it is the kinetic energy, not the momentum, that the rule adds. The kinetic energy is the one of the orbital law. With the kinetic energy $E - mc^2$ of Hypothesis 2 that a static clock would measure for the falling body, $mc^2\,(1/R - 1)$, the same rule would give $R = 1/(1 + u + u^2/2)$ instead, with the same expansion to second order and a faster decrease at large u; that form is not the one adopted.

For a uniform sphere of mass M and radius R_s the source term is

$$S(r) = \frac{M\left(3R_s^2 - r^2\right)}{2R_s^3} \quad (r \le R_s), \qquad S(r) = \frac{M}{r} \quad (r \ge R_s), \tag{42}$$

which is continuous at $r = R_s$. Three checks follow from (41): coincident clocks read alike, the comparison is continuous at the surface, and it tends to 1 when $M \to 0$ with λ fixed. A clock at the centre compared with one at the surface gives, to first order, $d\tau(0)/d\tau(R_s) = [\lambda + M/R_s]/[\lambda + 3M/(2R_s)] < 1$, whereas the source ratio is $3/2$. The conventional potential per unit mass of the sources is $\Phi = -G\,S$; the clock law uses S and the background λ directly, without a choice of potential zero. The background is held fixed within a domain; the model does not give a rule for the transition between domains with different dominant sources.

2.6 Bending of light in the gravitational field

Due to the time dilation effect, we expect to have different speed measurements of the same body by different observers. In particular, the speed-of-light traveling through the gravitational field will be different from the viewpoint of a local observer and the viewpoint of a distant watcher.

According to (38), a distant observer notes that the light beam has a velocity, which depends on the position in the gravitational field:

$$v = \frac{dr}{dt} = \frac{dr}{d\ell}\,\frac{d\ell}{d\tau}\,\frac{d\tau}{dt} = c\left(1 + \frac{2m_{sun}}{\lambda_g r} + \frac{2m_{sun}^2}{\lambda_g^2 r^2}\right)^{-1} \tag{43}$$

In this relation, τ is the time of a clock at r and ℓ the length read there on a material standard. The local speed $v_{local} = d\ell/d\tau = c = 2.998 \times 10^8\, m/s$ is constant due to our hypothesis (Hypothesis 1), and $d\tau/dt$ is the time rate (38). The remaining factor, $dr/d\ell$, equal to the time rate, is postulated (Table 1): the energy density of the superimposed potential lowers the speed of light by this factor, in addition to the factor of the time rate, and matter bound by the electromagnetic field scales by the same factor. A clock made of light between two material mirrors and an atomic clock at the same place then keep the same rate, as the comparison of cavity-stabilized oscillators with hydrogen masers over the variation of the potential of the Sun requires, to 1.7 parts in 100 of that variation [31]. The space itself remains constant: r is a distance in it, and it is matter, not space, that scales.

The distant observer can interpret the slow down of the light speed as the effect of some nonzero effective index of refraction:

$$n(r) \equiv \frac{c}{v} = 1 + \frac{2m_{sun}}{\lambda_g r} + \frac{2m_{sun}^2}{\lambda_g^2 r^2} \tag{44}$$

The deflection below is computed to first order in $m_{sun}/(\lambda_g r)$, which requires $\left\| \frac{m_{sun}}{\lambda_g} \right\| \ll r$. As we will see later, this condition is fulfilled for the majority of real astrophysical objects.

The ray is followed with one propagation law. Its speed is the distant-observer speed (43), $v = c/n(r)$, and its direction $\hat{t}$ turns by the refraction of the index $n(r)$ alone:

$$\frac{d\hat{t}}{dt} = v\,\nabla_\perp \ln n, \tag{45}$$

where $\perp$ denotes the component perpendicular to $\hat{t}$. This is the ray of least time for the speed (43), and no Newtonian acceleration acts on it. The postulate is the second factor of that speed (Table 1): the clock law alone gives half of the deflection and of the delay below, so the agreement of the totals with the measurements is a consistency of the model so completed, not an independent prediction. Both factors carry the background of the time rate, μ_g (Sec. 2.2.1), written λ_g since the two are equal in the solar system. For a ray of impact parameter b, with $r^2 = z^2 + b^2$ along the unperturbed path and to first order in $m_{sun}/(\lambda_g r)$, each of the two factors turns the ray toward the Sun by

$$\frac{m_{sun}}{\lambda_g}\int_{-\infty}^{\infty} \frac{b\,dz}{(z^2+b^2)^{3/2}} = \frac{2m_{sun}}{\lambda_g b}, \tag{46}$$

the deflection that the equivalence principle gives through the time dilation alone [13, Sec. 3.3.2]. For a ray grazing the Sun, $b = r_{sun}$, the total deflection angle is as follows:

$$\delta = \frac{4m_{sun}}{\lambda_g r_{sun}}\,, \tag{47}$$

where r_{sun} is the impact parameter, or the minimal distance from the light ray to the source of gravity. It has the form of the result derived by Einstein [14]; here half of it follows from the clock law, and the other half from the postulated second factor of (43).

The observed value of the deflection angle equals to (see [33], [34])

$$\delta_{obs} = \frac{4Gm_{sun}}{c^2 r_{sun}} = 0.847 \times 10^{-5}\,\text{rad} \tag{48}$$

General Relativity and Finite Theory reach the observed value (48) in different ways:

1. In General Relativity, whose time dilation corresponds to $\lambda_g = c^2/G = 1.35 \times 10^{27}\, kg/m$, the second half comes from the spatial part of the metric, the additional length contractions in the gravitational field explained in [13, Sec. 6.2.1].
2. In Finite Theory, we are decomposing the deflection angle into the time rate and energy density constituents:

$$\delta = \frac{2m_{sun}}{\lambda_g r_{sun}} + \frac{2m_{sun}}{\lambda_g r_{sun}} = \frac{4m_{sun}}{\lambda_g r_{sun}}\,, \tag{49}$$

With the solar-system value $\lambda_g = c^2/G$ (11), (49) equals the observed deflection (48). Each constituent is the discrepancy δ of (7).

The space is not contracted in this case: the second half comes from the energy density, with which matter scales.

The light speed (43) also determines the propagation delay. With $v = c/n$ and $\lambda_g = c^2/G$, a ray passing the Sun between distances r_1 and r_2 from it is delayed by $(2Gm_{sun}/c^3)\ln(4r_1r_2/b^2)$ to first order, the delay of General Relativity: in the parametrized post-Newtonian form $(1+\gamma)(Gm_{sun}/c^3)\ln(4r_1r_2/b^2)$ this is $\gamma = 1$, and the Cassini measurement gives $\gamma - 1 = (2.1 \pm 2.3) \times 10^{-5}$ [34]. The time rate alone, without the second factor, gives half of this delay ($\gamma = 0$), which that measurement excludes. To first order the index (44), $1 + 2m_{sun}/(\lambda_g r)$, is that of [16] and of General Relativity [13, Sec. 6.2.1], so that the bending and the delay of light do not distinguish the model from General Relativity at this order; the difference is of second order, of relative size at most of the order of $Gm_{sun}/(c^2 b)$, about 10^{-6} for a ray near the Sun, below the precision of that measurement.

2.7 Perihelion shift

The bending of light and perihelion shift of planets are the two classical tests of General Relativity. As we have seen in the previous subsection, the bending of light is

reproduced by the light speed (43) of the Finite Theory within a constant space. In this section, we consider the possibility of the Finite Theory to reproduce the perihelion shift of planets.

As we know, the radial motion of planets in the gravitational field of the Sun in Newton's gravity can be described by the relation

$$\frac{m\dot{r}^2}{2} + V(r) = \mathcal{E}\,, \tag{50}$$

where $V(r)$ is defined by

$$V(r) = -\frac{Gmm_{sun}}{r} + \frac{L^2}{2mr^2} \tag{51}$$

Here, m is the mass of the planet, m_{sun} — the mass of the Sun, E — the full non-relativistic energy of the planet, and L is the value of conserved angular momentum. Variable $r = \|\vec{r}\|$ is the distance to the Sun, which is supposed to be situated in the center of a coordinate system, and the dot means differentiation with respect to t. The second term in $V(r)$, in contrast to the attractive Newton's potential (first term), describes the action of repulsive centrifugal forces.

The general-relativistic investigation of the trajectory of a massive object in the spherically-symmetric gravitational field can also be described in terms of the effective gravitational potential (see, for example, [13]):

$$\frac{m\dot{r}^2}{2} + V_{eff}(r) = E\,, \tag{52}$$

In the model, the orbit combines the Newtonian acceleration with the time dilation. The effective potential of General Relativity is

$$V_{eff}(r) = -\frac{Gmm_{sun}}{r} + \frac{L^2}{2mr^2}\left(1 - \frac{2Gm_{sun}}{c^2 r}\right) \tag{53}$$

and the model keeps its Newtonian term and replaces the factor of the angular term by the square of the clock rate (38), which agrees with it to first order (10):

$$V_{eff}(r) = -\frac{Gmm_{sun}}{r} + \frac{L^2}{2mr^2}\left(1 + \frac{2m_{sun}}{\lambda_g r} + \frac{2m_{sun}^2}{\lambda_g^2 r^2}\right)^{-1} \tag{54}$$

The orbital law of the model is (54) in the radial energy (52), with one evolution parameter s for both coordinates and the angular law $d\varphi/ds = h/r^2$, where $h = L/m$ is conserved; this law is adopted (Table 1). As in the general-relativistic calculation of [13, Sec. 6.3 and Boxes 6.3–6.4], s is the proper time τ of the planet: $h = r^2\, d\varphi/d\tau$ and the energy are its constants of motion, the dot in (52) is $d/d\tau$, and (52) with (54) is the energy equation (6.41) of [13] with the factor $1 - 2Gm_{sun}/(c^2 r)$ of its centrifugal term replaced by the square of the clock rate. Eliminating this common parameter between the radial and angular laws gives the orbit $r(\varphi)$, and hence (57); a different parameter

would also require correspondingly transformed evolution equations. Differentiating the radial energy at fixed h gives, to first order in $m_{sun}/(\lambda_g r)$,

$$\frac{d^2r}{ds^2} = -\frac{Gm_{sun}}{r^2} + \frac{h^2}{r^3} - \frac{3m_{sun}h^2}{\lambda_g r^4}, \tag{55}$$

and with $u = 1/r$ and the angular law,

$$\frac{d^2u}{d\varphi^2} + u = \frac{Gm_{sun}}{h^2} + \frac{3m_{sun}}{\lambda_g}\, u^2. \tag{56}$$

For the unperturbed ellipse $u_0 = (1 + e\cos\varphi)/p$, with $p = h^2/(Gm_{sun}) = a(1-e^2)$, the resonant part of the last term shifts the frequency of the radial oscillation by $\varepsilon = 3m_{sun}/(\lambda_g p)$, and the perihelion advances per revolution by $2\pi\varepsilon$, as in Box 6.4 of [13] with $r^* = 2m_{sun}/\lambda_g$, which with $\lambda_g = c^2/G$ is

$$\delta\varphi = \frac{6\pi G m_{sun}}{c^2 a(1-e^2)}\,, \tag{57}$$

where a is the semi-major axis of the orbit and e is its eccentricity.

We know (see [33], [34]) that the perihelion shift agrees with observational evidence not only for Mercury but for all planets of the solar system. This leading result coincides with that of General Relativity. It is derived within the adopted orbital law; deriving that law, with its angular law and its time parameter, from a single action is not done here, and the expansion is kept to first order in $m_{sun}/(\lambda_g r)$.

To that order the adopted law agrees with the clock law and the light speed read together as a line element, $c^2 d\tau^2 = R^2 c^2 dt^2 - R^{-2}\left(dx^2 + dy^2 + dz^2\right)$, with R the rate (40) and cR^2 the light speed (43), the same in all directions. In the parametrized post-Newtonian form [34], $R^2 = 1 - 2u + 2\beta u^2$ and $R^{-2} = 1 + 2\gamma u$ with $u = Gm_{sun}/(c^2 r)$, this line element has $\gamma = 1$ and $\beta = 1$. A body on its path of extremal proper time advances its perihelion by $(2 + 2\gamma - \beta)/3$ of (57), the whole of it, and to first order that path obeys the adopted law itself, (52) with (54) and the angular law, when the radial coordinate of that law is read as $r + Gm_{sun}/c^2$. With the ratio $\lambda_g/(\lambda_g + m_{sun}/r)$ of the first published version as the clock rate, $\beta = 3/2$: the path gave five sixths of the observed advance and the adopted law the whole, so that the two disagreed; the second-order term of (40) removes this disagreement (Sec. 8.6). That bodies follow this path is not among the hypotheses of Sec. 2.1, and the orbital law remains adopted.

2.8 GPS and time dilation cancellation altitude

The gravitational time dilation and the kinematic time dilation both play a role on GPS satellites. The former is affected by the altitude whereas the latter is affected by its speed. We will study here the correct altitude where both effects cancel out.

First, we consider time dilation cancellation altitude from the viewpoint of General Relativity.

2.8.1 Time dilation cancellation altitude in General Relativity

Consider the artificial satellite, rotating around the Earth in circular orbit with radius r_{orbit}. Due to the gravitational dilation of time [see (39)], a static observer at altitude $r_{orbit} > r_{earth}$ should feel an accelerated flow of time with respect to the static observer on the Earth (r_{earth} is the radius of the Earth):

$$\frac{\Delta\tau_{orbit}}{\Delta\tau_{earth}} = \sqrt{\frac{1-\frac{2Gm_{earth}}{c^2 r_{orbit}}}{1-\frac{2Gm_{earth}}{c^2 r_{earth}}}} \tag{58}$$

But the satellite is not static, it rotates with linear velocity v, which leads to an additional relativistic effect:

$$\frac{\Delta\tau_{v}}{\Delta\tau_{earth}} = \sqrt{1-\frac{v^2}{c^2}} \approx 1-\frac{v^2}{2c^2} \tag{59}$$

Here, we are using the low-velocity approximation ($v \ll c$), which is justified for real GPS satellites. As we can see, the relativistic effect is opposed to the gravitational one, which makes it possible to find altitude, at which time dilation is canceled.

The final relation, which takes into account both effects, can be written in the form:

$$\frac{\Delta\tau_{satellite}}{\Delta\tau_{earth}} = \sqrt{\frac{1-\frac{2Gm_{earth}}{c^2 r_{orbit}}}{1-\frac{2Gm_{earth}}{c^2 r_{earth}}}}\left(1-\frac{v^2}{2c^2}\right) \tag{60}$$

$$\frac{\Delta\tau_{satellite}}{\Delta\tau_{earth}} \approx 1+\frac{Gm_{earth}}{c^2 r_{earth}}-\frac{Gm_{earth}}{c^2 r_{orbit}}-\frac{v^2}{2c^2} \tag{61}$$

where the last approximate equality is valid in the Newtonian limit $r_{earth}, r_{orbit} \gg m_{earth}/\lambda_g$. Also, under these conditions we can use the Newtonian relation for the velocity of the satellite, rotating in a circular orbit $v^2 = Gm_{earth}/r_{orbit}$, which results in the relation:

$$\frac{v^2}{c^2} = \frac{Gm_{earth}}{c^2 r_{orbit}} \tag{62}$$

Consequently, the radius of the orbit, at which cancellation occurs, is found to be

$$\frac{\Delta\tau_{satellite}}{\Delta\tau_{earth}} \approx 1-\frac{3Gm_{earth}}{2c^2 r_{orbit}}+\frac{Gm_{earth}}{c^2 r_{earth}} = 1 \quad \Rightarrow \quad r_{orbit} = \frac{3r_{earth}}{2} \tag{63}$$

which corresponds to the altitude $H = r_{orbit} - r_{earth} = r_{earth}/2 \approx 3185\,km$ [2].

2.8.2 Time dilation cancellation altitude in Finite Theory

For the same artificial satellite, Finite Theory supposes the gravitational dilation of time for static observers to be defined, to first order in $m_{earth}/(\lambda_g r)$, by [see (38) and

(11)]

$$\frac{\Delta\tau_{orbit}}{\Delta\tau_{earth}} = \frac{1+\frac{m_{earth}}{\lambda_g r_{earth}}}{1+\frac{m_{earth}}{\lambda_g r_{orbit}}}\,, \qquad \lambda_g = \frac{c^2}{G} = 1.3466\times 10^{27}\, kg\, m^{-1} \tag{64}$$

where λ_g is the gravitoelectric constant of (11), as the circular-orbit relation (67) below requires. You'll notice above that the radii are swapped when compared to their GR counterpart (58). The satellites are in the comoving framework of the Earth ($y = 0.990$, Sec. 2.3), so their kinematic time dilation is the one relative to the Earth (see Sec. 2.5.1):

$$\frac{\Delta\tau_v}{\Delta\tau_{earth}} = \sqrt{1-\frac{v^2}{c^2}} \approx 1-\frac{v^2}{2c^2} \tag{65}$$

The gravitational time dilation of Finite Theory differs in form from that of General Relativity but agrees with it to first order in $m_{earth}/(\lambda_g r)$, and the kinematic effects are the same. By combining (64) and (65) we get

$$\frac{\Delta\tau_{satellite}}{\Delta\tau_{earth}} = \frac{\left(1+\frac{m_{earth}}{\lambda_g r_{earth}}\right)\left(1-\frac{v^2}{2c^2}\right)}{1+\frac{m_{earth}}{\lambda_g r_{orbit}}} \tag{66}$$

For the orbital velocity of the satellite we have $v^2 = Gm_{earth}/r_{orbit}$, which results in the relation

$$\frac{v^2}{c^2} = \frac{Gm_{earth}}{c^2 r_{orbit}} = \frac{m_{earth}}{\lambda_g r_{orbit}} \tag{67}$$

Setting $\Delta\tau_{satellite} = \Delta\tau_{earth}$ then gives

$$r_{orbit} = \frac{3\lambda_g r_{earth} + m_{earth}}{2\lambda_g} \tag{68}$$

The corresponding altitude $H = r_{orbit} - r_{earth} = r_{earth}/2 + m_{earth}/(2\lambda_g) \approx 3185\, km$ coincides with the altitude derived in Sec. 2.8.1 in the frames of General Relativity. For the GPS orbit itself, $r_{orbit} = 26\,562\, km$, (66) gives a gain of the satellite clock of $38.5\,\mu s$ per day, in agreement with the rate offset of $38.6\,\mu s$ per day built into the GPS satellite clocks [2]. This is a consistency check at leading order, not a validation of GPS timing, which also involves the reference timescale, the rotation of the Earth and the geoid, and orbital corrections.

2.9 Gravitational time dilation

The notion of gravitational time dilation is the simple relation between the gravitational potential energy at a given radius and the time rate at that radius. The potential energy of a mass m at a distance r from a mass M is $-GMm/r$: it varies as $1/r$. With (38), the time rate at r relative to a distant observer is

$$\frac{\Delta\tau}{\Delta t} \approx \left(1+\frac{M}{\lambda_g r}\right)^{-1} \approx 1-\frac{GM}{c^2 r} \tag{69}$$

with $\lambda_g = c^2/G$ in the solar system. The clock rate therefore rises with altitude by GM/c^2 times the decrease of $1/r$, as in General Relativity. This $1/r$ dependence was confirmed by the hydrogen maser of Gravity Probe A, carried to 10 000 km, to 7×10^{-5} [32], and by the two Galileo satellites on eccentric orbits to a few parts in 10^5 [15, 17]. In a static field such as that of the Sun, the energy of a freely moving body, measured by a distant observer, is conserved in both theories.

2.10 Gravitational redshift

From the previous subsection, a photon travelling up in altitude gains speed as seen by a distant observer, since the time rate $(1 + M/(\lambda_g r))^{-1}$ increases with altitude.

Why local observers will observe a gravitational redshift in frequency of the observed photon then? For the simple reason their own gravitational time rate factor will be accelerated as well, making the relative perception of the photon frequency accordingly altered (see Fig. 4).

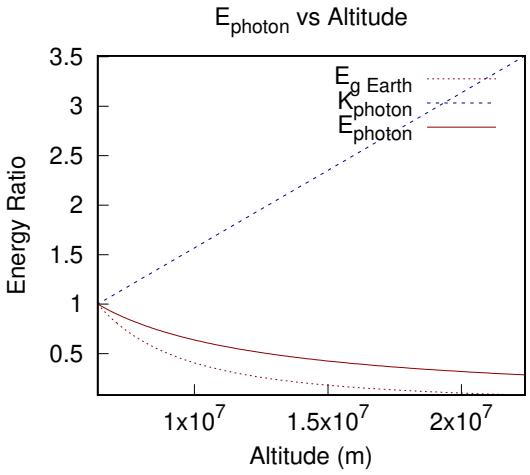

Fig. 4 Gravitational Redshift

Now as we know, the relativistic Doppler shift is given by the following formula:

$$f_o = \sqrt{\frac{1 - \frac{v}{c}}{\frac{v}{c} + 1}} \times f_f \tag{70}$$

In Finite Theory the Doppler shift seen by a moving observer is the classical shift $(1 - v/c)$ divided by the observer's kinematic time rate factor (35):

$$f_o = \frac{1 - \frac{v}{c}}{\sqrt{1 - \frac{v^2}{c^2}}} \times f_f = \sqrt{\frac{1 - \frac{v}{c}}{\frac{v}{c} + 1}} \times f_f \tag{71}$$

which is identical to the relativistic Doppler shift at all velocities.

To find the gravitational redshift and the relativistic Doppler shift cancellation point, we'll use the following formula:

$$\sqrt{\frac{\left(1-\frac{2G\,m_e}{c^2\,\|p_e-d\|}\right)\left(1-\frac{v}{c}\right)}{\left(1-\frac{2G\,m_e}{c^2\,\|p_e\|}\right)\left(\frac{v}{c}+1\right)}}=1 \tag{72}$$

Where:

- v is the relative velocity between the observer and the moving apparatus
- $c = 299792458\,m/s$
- $G = 6.67408\times10^{-11}\,m^3kg^{-1}s^{-2}$
- $d = 22.5\,m$ (elevation of the tower)
- $p_e = -6.371\times10^6\,m$ (position of the center of the Earth)
- $m_e = 5.973\times10^{24}\,kg$ (mass of the Earth)

Or:

$$v=\frac{Gcd\,m_e}{c^2\,\|p_e\|^2+(c^2d-2G\,m_e)\,\|p_e\|-Gd\,m_e} \tag{73}$$

$$v = 7.371\times10^{-7}\,m/s \tag{74}$$

$$v/c = 2.459\times10^{-15} \tag{75}$$

Now by using Finite Theory we'll have the following relation:

$$\frac{\left(\frac{m_e}{\|p_e\|}+\lambda_g\right)\left(1-\frac{v}{c}\right)}{\left(\frac{m_e}{\|p_e-d\|}+\lambda_g\right)\sqrt{1-\frac{v^2}{c^2}}}=1 \tag{76}$$

Where:

- v is the relative velocity between the observer and the moving apparatus
- $c = 299792458\,m/s$
- $G = 6.67408\times10^{-11}\,m^3\,kg^{-1}\,s^{-2}$
- $\lambda_g = 1.35\times10^{27}kg\,m^{-1}$
- $d = 22.5\,m$ (elevation of the tower)
- $p_e = -6.371\times10^6\,m$ (position of the center of the Earth)
- $m_e = 5.973\times10^{24}\,kg$ (mass of the Earth)

Or, neglecting the second-order term $v^2/c^2 \sim 10^{-30}$:

$$v=\frac{c\,m_e\,\|p_e-d\|-c\,m_e\,\|p_e\|}{\lambda_g\,\|p_e\|\,\|p_e-d\|+m_e\,\|p_e\|} \tag{77}$$

$$v = 7.371\times10^{-7}\,m/s \tag{78}$$

$$v/c = 2.459\times10^{-15} \tag{79}$$

We'll notice once again that by using completely different mathematics we obtain the same factors which correspond to observations [24].

2.11 Newton's gravitational constant

In Finite Theory, Newton's constant is $G = c^2/\lambda_g$ (15), and λ_g depends on the superimposed potentials (Sec. 2.5.3). Experimentally, G is the least precisely known of the fundamental constants. CODATA 2022 recommends $G = 6.67430(15) \times 10^{-11}\, m^3\, kg^{-1}\, s^{-2}$ (22 ppm), after the uncertainties of the input measurements were expanded by a factor of 3.9 to make them mutually consistent [22]. Recent high-precision measurements differ by several hundred ppm [25]. The BIPM torsion balance gave $6.67554(16) \times 10^{-11}\, m^3\, kg^{-1}\, s^{-2}$ in 2014, 186 ppm above the recommended value. The same balance, operated at NIST, gave $6.67387 \times 10^{-11}\, m^3\, kg^{-1}\, s^{-2}$ with an uncertainty of 57 ppm: 250 ppm lower, and within one standard deviation of the recommended value [26]. No single cause of the difference was identified [25].

A laboratory at latitude φ moves with the rotation of the Earth and carries the rotational kinetic potential $\Phi_{rot} = \frac{1}{2}(\omega R \cos\varphi)^2$, where $\omega = 7.292 \times 10^{-5}\, s^{-1}$ and R is the radius of the Earth. Compared with the gravitational potential $\Phi_g = Gm_{earth}/R$:

$$\frac{\Phi_{rot}}{\Phi_g} = \frac{\omega^2 R^3}{2Gm_{earth}} \cos^2\varphi = 1.72 \times 10^{-3} \cos^2\varphi \tag{80}$$

This is 750 ppm at Sèvres (48.83°N) and 1280 ppm at Wuhan (30.51°N): the same order of magnitude as the spread of the measured values of G.

To test whether this potential accounts for the spread, the measured value can be written as

$$G_{measured} = G_0 \left(1 - k\, \frac{\Phi_{rot}}{\Phi_g}\right) \tag{81}$$

Moving the BIPM balance from Sèvres to Gaithersburg (39.13°N) raised Φ_{rot}/Φ_g by 290 ppm, and the measured value fell by 250 ± 62 ppm, giving $k = 0.86 \pm 0.21$. Two other instruments using the same method, angular acceleration feedback, gave $6.674484(78) \times 10^{-11}\, m^3\, kg^{-1}\, s^{-2}$ at Wuhan (HUST-18) and $6.674255(92) \times 10^{-11}\, m^3\, kg^{-1}\, s^{-2}$ at Seattle (UWash-00, 47.65°N) [35]. With $k = 1$ the Wuhan value would be 498 ppm lower; it is 34 ± 18 ppm higher, giving $k = -0.07 \pm 0.04$. The two values of k differ by 4.3 standard deviations. Instruments at almost the same latitude also differ, BIPM-14 and UWash-00 by 193 ppm, so the spread is not set by latitude alone.

The rotational kinetic potential therefore matches the size of the discrepancy in G, but a single dependence on latitude does not fit all the measurements. Operating one apparatus at a third latitude would test the dependence directly.

3 Nuclear implication

3.1 Newtonian or Coulombian Forces

If we integrate time dilation into the Newtonian or Coulombian acceleration then we'll have the following construction. It is stated for two identical particles of signed charge q_e at separation $x > 0$, with an electric background λ_e, a linear charge density in C/m whose value is not fixed here, in the role that λ_g has in (38):

$$f_e = \frac{\lim_{s\to\infty} \frac{q_e}{s} + \lambda_e}{\frac{q_e}{x} + \lambda_e} \tag{82}$$

With the observer at infinity, $f_e = \lambda_e/(q_e/x + \lambda_e) = x/(x + a)$, with $a = q_e/\lambda_e$ and $\lambda_e \neq 0$. The factor keeps this ratio, the first-order form of the clock rate (40); the second-order term of that rate is not carried into the hypothesis of this section, Hypothesis 5 being stated for the gravitational potential only. The admissible domain is $x > 0$ when $a > 0$, and $x > |a|$ when $a < 0$, where $x+a$ would otherwise vanish. First let's write the potential energy as the integral of the force with respect to position, with its reference at infinity, $u_e(\infty) = 0$, so that $u_e = Kq_e^2/x$:

$$u_e = -Kq_e^2 \int \frac{1}{x^2} dx \tag{83}$$

The hypothesis of this section is that the interaction energy of the pair is $f_e^2 u_e$, the square of the time dilation factor applied to the potential energy, given the equivalent dimensions. With the conventional sign, a positive force pushing the particles apart, the force is the negative derivative of this energy with respect to the separation:

$$F_e = -\frac{d}{dx}\left(f_e^2 u_e\right) = Kq_e^2 \frac{x - a}{(x + a)^3} \tag{84}$$

Because the energy depends only on the separation, the forces on the two particles are equal and opposite, $F_1 = -U'(x)\,\hat{x}$ and $F_2 = +U'(x)\,\hat{x}$ with $U = f_e^2 u_e$ and $\hat{x}$ the unit vector from particle 2 to particle 1, and the momentum of the pair is conserved; a field carrying the interaction would add its own momentum, which is not treated here. For $x \gg |a|$ the force tends to the Coulomb repulsion Kq_e^2/x^2. For $a > 0$ it changes sign at $x = a$, where the energy has its maximum $Kq_e^2/(4a)$, and it is attractive below. The reference is part of the hypothesis: replacing u_e by $u_e + C$ before multiplying by f_e^2 adds the force $-2Cax/(x+a)^3$. How two different charges would enter is not specified.

The interaction energy is an additional hypothesis (Table 1): the value of λ_e is not fixed, and the force law has not been evaluated against nuclear data.

4 Cosmological implications

The results of this section are conditional: each follows from the hypotheses of Sec. 2.1 together with the further assumptions stated where it is introduced, and none is an independent test of the model. They are conjectures, given with the differences from GR that they would imply. Given the measured bending of light, the parameters of larger structures can be inferred, or "reverse engineered", under these assumptions.

At this level, only complex computer research can be proposed to simulate modeling of the universe under this umbrella to match its behavior with measurements such as the constant of Hubble's Law. Potentially, simulators can also be used to reverse time and estimate an early universe according to the current velocities of the superclusters, solve the scaling factor of the observed universe which will lead to an estimation of the real volume of the universe, and solve local focal points of gravitational lenses.

4.1 Natural faster-than-light speed

One of the most practical and interesting goals of any research area in this field is to reach exoplanets. Unfortunately, since GR disallows any probe or ship to travel faster than c we reach an impasse because one of the closest star named Alpha Centauri is about $4.36507\,ly$ or $4.01345 \times 10^{16}\,m$ away from us. This means light rays will take $4.36507\,years$ to overtake that distance according to GR. The following section explores the consequences of FT on close distances such as the Moon that will follow the following principle:

$$t = \int \frac{\sum_{i=1}^{n} \frac{m_i}{\|x-d_i\|} + \lambda_g}{\sum_{i=1}^{n} \frac{m_i}{\|d_i\|} + \lambda_g} \times \frac{1}{c} dx \tag{85}$$

Here x is the distance read on material standards. The light speed (43) and the scaling of matter of Sec. 2.6 leave this principle as it is: over an element $dr = R\,dx$ of the constant space, with R the rate (40), light takes $dr/(cR^2) = dx/(cR)$ of the distant time, which the clock of the observer, of rate R_o, reads as $R_o\,dx/(cR)$, the integrand above to first order in S/λ.

4.1.1 Moon

To estimate the distance of the Moon in conformance to FT, we will follow the henceforth equation that takes into account the adjoining most massive entity, or the influence of the scaling factor. We also know the time it takes for a laser to travel back and forth between the Moon and the surface of the Earth. Once again the scaling factor represents the average influence of all surrounding stars.

The light path runs from the observer on the Earth's surface ($x = 0$) to the lunar surface ($x = x_{ft} - r_m$), with the centre of the Earth behind the observer and the Moon and the Sun ahead of the path. Integrating each term of the principle above along this path gives:

$$\begin{aligned} 1.25\,s = & \frac{\lambda_g\,(x_{ft} - r_m) + m_e \log\left(\frac{x_{ft}-r_m-p_e}{\|p_e\|}\right)}{c\left(\frac{m_m}{\|x_{ft}\|} + \frac{m_s}{\|p_s\|} + \frac{m_e}{\|p_e\|} + \lambda_g\right)} \\ & + \frac{m_s \log\left(\frac{p_s}{p_s - x_{ft} + r_m}\right) + m_m \log\left(\frac{x_{ft}}{r_m}\right)}{c\left(\frac{m_m}{\|x_{ft}\|} + \frac{m_s}{\|p_s\|} + \frac{m_e}{\|p_e\|} + \lambda_g\right)} \end{aligned} \tag{86}$$

And after numerical analysis we'll find that:

$$x_{ft} = 3.7647807274 \times 10^8\,m \tag{87}$$

Where:

- $c = 299792458\,m/s$
- $G = 6.67408 \times 10^{-11}\,m^3 kg^{-1} s^{-2}$
- $\lambda_g = c^2/G = 1.35 \times 10^{27}\,kg/m$

- $p_e = -6.371 \times 10^6\, m$ (position of the center of the Earth)
- $m_e = 5.973 \times 10^{24}\, kg$ (mass of the Earth)
- $r_m = 1.7375 \times 10^6\, m$ (radius of the Moon)
- $m_m = 7.348 \times 10^{22}\, kg$ (mass of the Moon)
- $p_s = 1.52 \times 10^{11}\, m$ (position of the center of the Sun)
- $m_s = 1.98892 \times 10^{30}\, kg$ (mass of the Sun)

If we compare with a flat-propagation baseline, which is not a complete lunar-ranging calculation in General Relativity:

$$x_{gr} = c \times 1.25 + r_m \tag{88}$$

$$x_{gr} = 3.764780725 \times 10^8\, m \tag{89}$$

Which is a difference of:

$$x_{ft} - x_{gr} = 0.24\, m \tag{90}$$

The difference comes almost entirely from the potential of the Earth, which decreases along the path ($+0.243\, m$); the Sun and the Moon contribute $-4.5\, mm$ and $-0.2\, mm$. It corresponds to an average speed of light along the path exceeding the value c measured at the observer by $6.4 \times 10^{-10}\, c$. It is not an established discrepancy from General Relativity: that comparison needs a common coordinate convention, the station and reflector geometry and motion, and the gravitational propagation corrections.

4.2 Earth's Tides and Flyby Anomaly

It is important to point out also that a deep study of the microgal as measured in various places around the Earth [7] gives consistent results in the residual, or the difference between the theoretical and measured gravitational acceleration; one record is shown in Fig. 5 and 6:

Since the normalized residual is proportional to the normalized derivative of the theoretical gravitational acceleration, it is compatible with an æther wind (or comoving superimposed gravitational framework) given the preferred alignment of the gravimeter; towards or perpendicular to the Sun. A timing or phase offset τ between the tide model and the record produces the same signature, since $g(t + \tau) - g(t) \approx \tau\, \dot{g}(t)$; an ocean-loading lag or a timestamp offset has to be excluded before the residual is attributed to an æther wind.

Lastly, it was recently found that the famous flyby anomaly is directly proportional to the Earth's rotation [18] which is consistent with the Earth's tides or an æther wind.

4.3 Parameters of the invisible universe

4.3.1 Galactic rotation curve

The laws of classical physics imply there is a parent framework from which rotating stars relate to in all cases. But what if we have a universe with only one black hole in it? The black hole will rotate relative to which comoving framework?

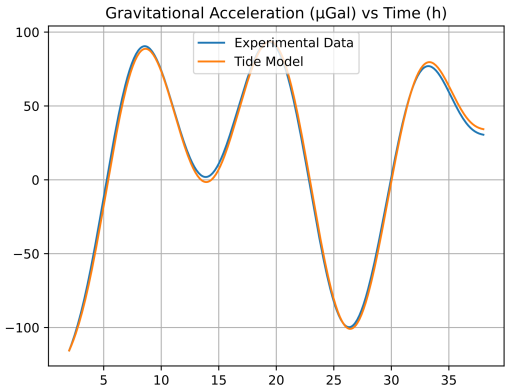

Fig. 5 Microgal vs Time

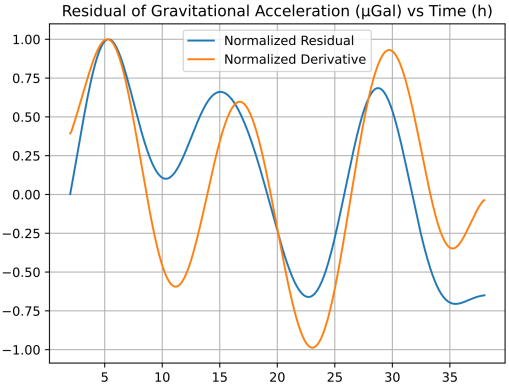

Fig. 6 Microgal Residual vs Time

We can see here that the black hole cannot rotate if it is the sole one in the universe. This singular black hole will be the one defining the absolute framework from which other stars will rotate around and their planets will rotate around each one of these stars, and so on. So the comoving frameworks simply are superimposed with the most massive body defining the absolute one.

The rotation curve illustrates this property because of the huge mass involved at the center of galaxies. Given that mass, each galaxy has its own comoving framework (Definition 1), rotating at an angular velocity ω: the stars move with that framework, the term ωx, and orbit the bulge within it. The term ωx is treated as a physical streaming of the stars with that framework, added to their orbital speed; the measured speeds are used as given, without transforming them to another frame. The streaming is taken as the rotation of the framework itself (Definition 1); no force maintaining it is specified, and in the fits the term is empirical. If we take for example the formula

of a standard rotation curve as given by the following equation, which is the standard orbital speed but affected by the time dilation, the clock rate (40), and its comoving superimposed gravitational framework:

$$v = \omega x + \frac{\lambda_g \sqrt{\frac{Gm}{x}}}{\sqrt{\left(\frac{m}{x} + \lambda_g\right)^2 + \left(\frac{m}{x}\right)^2}} \tag{91}$$

Where:

- v is the tangential velocity of the stars
- ω is the angular velocity of the comoving framework of the galaxy
- $G = 6.67408 \times 10^{-11}\, m^3 kg^{-1} s^{-2}$
- $\lambda_g = [1 \times 10^{18}, 1 \times 10^{22}]\, kg\, m^{-1}$
- m is the mass of the bulge in the model, a fitted parameter and not an independent measurement
- x is the distance from the center of the galaxy

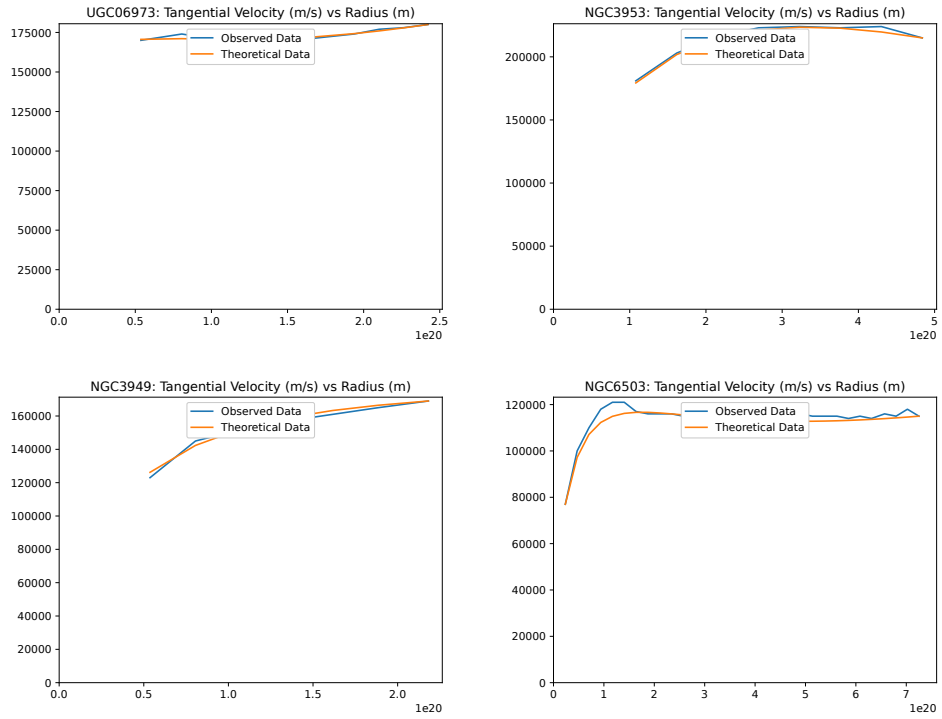

Fig. 7 Rotation Curve

So after retrofitting 497 curves of 486 galaxies (Fig. 7 & 8), with a mean standard deviation of $7900\, m/s$, we observe a linear mass density with a median of

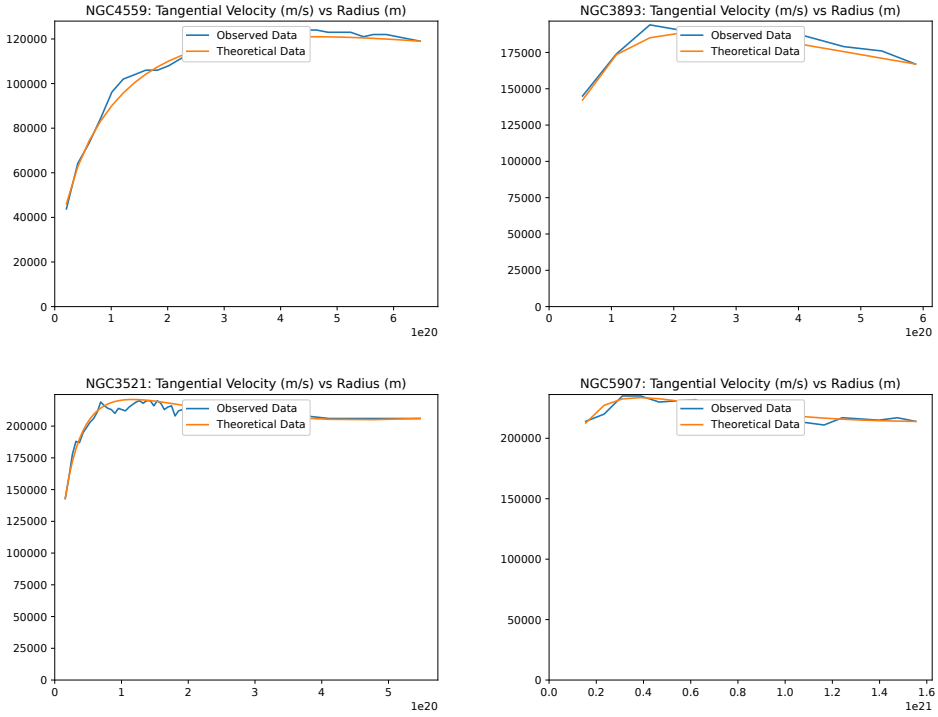

Fig. 8 Rotation Curve

$1.9 \times 10^{21}\, kg\, m^{-1}$ (quartiles 0.90 and 3.2×10^{21}), of the order of the $4.1 \times 10^{21}\, kg\, m^{-1}$ fitted below for the Milky Way.

This is a fit, not a derivation. The data are the 175 rotation curves of SPARC [20] and 322 curves of the atlas of [27], 497 curves in all; eleven objects appear twice, nine in both sets and two within the atlas, so the curves cover 486 galaxies. For each curve, λ_g, m and ω of (91) are fitted: λ_g on a grid from 10^{18} to $10^{22}\, kg/m$, m between 1/15 and 15 times a photometric mass scale, and ω, the angular velocity of the comoving framework of the galaxy, so that the curve passes through the last measured point. The model does not predict the value of ω, so it counts as a fitted parameter; it is positive in 369 of the 497 fits and negative, a framework turning against the stars, in 128; its median over all fits is $0.97\, km\, s^{-1}\, kpc^{-1}$. The objective is the standard deviation of the residuals about their mean, not weighted by the measurement errors, so a constant offset of the curve is not counted. The deviation quoted, 7949 m/s, is the mean of this standard deviation over the 497 curves (median 6297 m/s); the root-mean-square residual, which counts the offset, averages 10 485 m/s. On the same curves, with the same objective and three parameters, an empirical arctangent curve with the same linear term averages 6255 m/s, and the Newtonian limit of (91), $\lambda_g \to \infty$, a central mass with the same linear term and not a model of the stellar disc and gas, averages 67 795 m/s. The fits depend on the form of the clock rate, because $m/(\lambda_g x)$ is not small in them: over the curves its median is 0.3 at the outermost point and 25 at

the innermost. With the ratio $\lambda_g/(m/x + \lambda_g)$ of the first published version in place of the rate (40), the same procedure averages 8031 m/s (median 6526 m/s); with the exponential $e^{-m/(\lambda_g x)}$, which has the same expansion to second order as (40), it averages 10 539 m/s (median 8706 m/s). The solar-system tests fix the rate to second order only, and the form (40) was chosen after these fits (Sec. 2.5.4). At large x the second term of (91) tends to $\sqrt{Gm/x}$, so the curve tends to ωx, or declines when $\omega = 0$: the fits describe the measured range of each curve, out to a median radius of 31 kpc, and do not give an asymptotically flat law. They are empirical, finite-range fits with their freedom stated; no conclusion that dark matter is observationally excluded follows from them alone. The fitted parameters of every curve and the scripts are in [9].

The Milky Way is not among these curves. Fitted by the same procedure to the curve of [28] outside the bulge, 39 points from 2.6 to 95.6 kpc, with the stellar mass of the Galaxy, $5 \times 10^{10}\, M_\odot$ [5], as the mass scale, (91) gives $\lambda_g = 4.1 \times 10^{21}\, kg\, m^{-1}$ (3.7 to 4.6×10^{21} within 10 % of the minimum standard deviation) and $m = 4.5 \times 10^{11}\, M_\odot$, with a standard deviation of 7.6 km/s and a root-mean-square residual of 11.3 km/s (6.7 and 8.0 km/s, at $3.5 \times 10^{21}\, kg\, m^{-1}$, with the ratio of the first published version); for inner limits from 2 to 5 kpc, λ_g stays between 4.10 and $4.30 \times 10^{21}\, kg\, m^{-1}$. This inner limit was chosen after inspecting the fits: over the whole curve, from 0.1 kpc, the single central mass of (91) does not follow the peak of the bulge at 0.4 kpc, and the fit gives $1.65 \times 10^{21}\, kg\, m^{-1}$ with a standard deviation of 34 km/s and a root-mean-square residual of 102 km/s.

4.3.2 Position of the Universal Core

Assuming that Hubble's constant represents the time rate of a greater encompassing and invisible entity, the gravitational acceleration of the visible universe follows from that constant, $H_0 = 2.26 \times 10^{-18}\, s^{-1}$:

$$a_{universe} = H_0 c \tag{92}$$

$$a_{universe} = 6.7753 \times 10^{-10}\, m/s^2 \tag{93}$$

To find the position of the universal core the visible universe of traveling away from, we'll need to start with the following definitions, with the standard definition of Newtonian gravitational acceleration:

$$a_{universe} = \frac{G\, M_{core}}{{s_{core}}^2} \tag{94}$$

And the definition of G, according to Finite Theory:

$$G = \frac{c^2}{\lambda_{g,\text{invisible}}} \tag{95}$$

Plus the fact that the only large-scale entity at that level is the universal core then:

$$\lambda_{g,\text{invisible}} = \frac{M_{core}}{s_{core}} \tag{96}$$

We'll have the acceleration of the visible universe inversely proportional to the position of the universal core:

$$a_{universe} = \frac{c^2}{s_{core}} \tag{97}$$

Now by using (93), we'll have:

$$6.7753 \times 10^{-10}\, m/s^2 = \frac{c^2}{s_{core}} \tag{98}$$

Where the position of the universal core can be solved with:

$$s_{core} = 1.3265 \times 10^{26}\, m \tag{99}$$

Under this assumption, the distance we are away from the universal core would be $1.3265 \times 10^{26}\, m$. Substitution gives $s_{core} = c/H_0$: the result restates the assumptions $a_{universe} = H_0 c$ and $G = c^2/\lambda_g$ and is not independent evidence for a universal core, its position or its mass.

5 Laboratory experiments

Six bench experiments made with the author's own apparatus are reported here: the free fall of a magnetized sphere, a pendulum comparing magnets with a steel sphere, a magnet floating on water, the weight of a block magnet with either face up, the apparent weight of a spinning disc on a beam balance, and a liquid-gallium vortex. Each is given with its method, its measured statistics and its status; no model is fitted to explain them. Table 2 summarizes the status of each.

5.1 Free fall of a magnetized sphere

5.1.1 Method

A 66 g NdFeB sphere and a 66 g steel sphere, both 25 mm in diameter, were dropped together, about 57 cm apart, and filmed at 240 frames per second. Forty paired drops were made in five sessions (days 7 to 11), four in each orientation of the magnet, with its axis vertical in two opposite orientations labelled U and D. The positions of both spheres were tracked every 62.5 ms over the first 0.75 s of each drop. A wall stands close to the upper half of the path, so the results below use the lower half of each fall, away from it. Each fall was fitted with a constant acceleration in each half of the drop, a_1 above mid-height and a_2 below it, with the position and velocity continuous at mid-height. The release height and velocity are free, which removes offsets of the release position and velocity from the fitted accelerations, though not frame-timing errors, nonquadratic image distortion, early release transients or correlated tracking errors; the continuity at mid-height lets the whole track fix the speed at which the sphere enters the lower half.

The lower half is also where the video distorts most: there the apparent acceleration of the steel sphere is $14\, m/s^2$. Each drop is therefore calibrated on its steel sphere, whose fall is known: a scale that changes linearly with height is fitted to the steel track,

Table 2 Status of the bench experiments

Experiment	Measured	Status
Free fall	Under the adopted steel-reference calibration, fitted acceleration of the magnet 21 ± 4 % below the reference over the lower half of the drop and 15 ± 1 % over the upper half; calibration-transfer uncertainty not included	Open; not identified as a physical free-fall anomaly
Pendulum	Period of the magnets 0.80 ± 0.03 % longer than that of the steel sphere, 0.47 to 0.53 % after estimated corrections	Open; conditional equivalent m_g/m_i of 0.989 to 0.991 if the effective lengths are equal and the non-gravitational torques unchanged
Floating magnet	Drift of 1 to 7 mm/s (afternoon values upper bounds) in a direction that changes between runs; on a plastic support, with no steel under the container, one block west and two blocks east from the same starting point; none without the magnet	Open; cause not identified, ordinary interactions not excluded, no new force established
Magnet weight	Block magnet read at 93.925 g and 94.056 g with either face up (0.131 g); 0.1 ± 0.03 g over the 20 weighings; no reading with the block held above the pan	Open; apparent anomaly under investigation; a non-uniform ambient field at the magnet not excluded, no new force established
Spinning disc	Speed-dependent load changes: sign changes below about 2400 rpm and apparent lightening above, some readings limited by the beam stops or a transferred calibration	Open; air flow, vibration and lead forces not excluded
Gallium vortex	2.6 ± 3.7 g	Inconclusive

taking its true fall as g less the 0.36 % air drag expected for both spheres, which have the same size and mass but not necessarily the same surface, rotation or surroundings ($9.77\,m/s^2$), and applied to the magnet's track. The fit to the steel sphere cannot itself verify that the same scale holds at the position of the magnet in the image. In one drop (day 8, D) the steel track fails, at $6.9\,m/s^2$, and that drop is excluded, leaving 39 (Table 3). The per-session summary in [11] fits the median of the four drops of a block with the release height fixed at zero; because the first tracked position lies 2 to 5 cm below the origin, that fit is biased, and it is not used here.

5.1.2 Results

With the adopted steel-reference calibration, the fitted lower-half acceleration of the magnet is $7.71 \pm 0.41\,m/s^2$, $2.06 \pm 0.41\,m/s^2$ (21 ± 4 %) below the $9.77\,m/s^2$ reference value. The $\pm 0.41\,m/s^2$ is the standard error of the mean of the 39 drops and describes their statistical scatter; it does not include the uncertainty of transferring the calibration from the track of the steel sphere to that of the magnet, 57 cm away in the image, which has not been propagated. The other ways of handling the distortion bracket this value: correcting instead for a clock that runs unevenly gives 25 ± 4 %, and the ratio of the two spheres' accelerations over the same lower half, without calibration, gives 18 ± 3 %. These are sensitivity checks on the same data, not independent validations

Table 3 Accelerations of the NdFeB sphere in the upper and lower halves of the drop, calibrated on the steel sphere: mean and standard error of the drops in each session block

Block	Drops	a_1, upper half (m/s^2)	a_2, lower half (m/s^2)
Day 7, U	4	8.16 ± 0.21	5.00 ± 1.19
Day 7, D	4	8.88 ± 0.31	6.70 ± 1.55
Day 8, U	4	8.33 ± 0.38	7.44 ± 1.59
Day 8, D	3	8.74 ± 0.10	7.61 ± 0.89
Day 9, U	4	7.10 ± 0.55	7.24 ± 0.68
Day 9, D	4	8.46 ± 0.04	8.64 ± 1.34
Day 10, U	4	8.00 ± 0.57	8.36 ± 0.71
Day 10, D	4	8.57 ± 0.29	8.91 ± 1.83
Day 11, U	4	8.07 ± 0.46	9.28 ± 1.60
Day 11, D	4	8.80 ± 0.34	7.91 ± 1.05

of the calibration on which the deficit rests. In the upper half, beside the wall, the fitted deficit is $15 \pm 1\,\%$, so the fitted deficit is at least as large away from the wall as beside it. With about four tracked positions per sphere in the lower half, each drop gives its lower-half acceleration to about $\pm 2.6\,m/s^2$, against ± 0.4 to $1.0\,m/s^2$ over the whole fall.

Each day gives one U block and one D block, so the lower-half accelerations separate into a part common to both orientations, $-2.06 \pm 0.51\,m/s^2$, and a part that reverses with orientation, $+0.25 \pm 0.27\,m/s^2$ (Fig. 9), with standard errors from the scatter of the five days, which treat each day, not each drop, as one measurement and so differ from the drop-based $\pm 0.41\,m/s^2$ above. The reversing part is consistent with zero in the lower half; in the upper half, beside the wall, it is $+0.38 \pm 0.08\,m/s^2$, positive on all five days. In the lower half the magnet also accelerates sideways, away from the steel sphere: relative to it, by $0.42 \pm 0.09\,m/s^2$ in the D drops and $0.89 \pm 0.20\,m/s^2$ in the U drops. The compass direction of this motion was not recorded.

5.1.3 Status

Open. Under the adopted steel-reference calibration the fitted lower-half acceleration of the magnet is about 21 % below the reference value; the quoted ± 4 percentage points describe the statistical scatter and do not include the unresolved calibration-transfer uncertainty, so the deficit is not identified as a physical free-fall anomaly. The fitted deficit remains in the lower half, away from the wall, with its cause unresolved. The magnetic attraction between the magnet and the steel sphere that it magnetizes, $4 \times 10^{-8}\,m/s^2$ at 57 cm, is too small to contribute; this does not bound the coupling of the magnet to other steel or to conductors near its path. The conditional mass-ratio equivalent of the pendulum of Sec. 5.2 differs from 1 by about 1 %, much less than the deficit. Mapping the camera response at both trajectories, exchanging the positions of the two spheres, dropping an unmagnetized sphere of the same material, and dropping the magnet alone away from conductors would each test one of these effects.

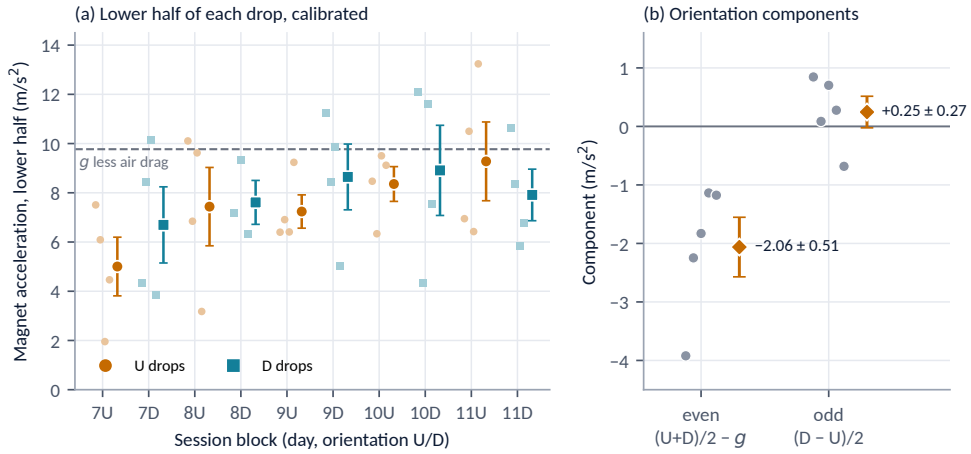

Fig. 9 Free fall of a 66 g NdFeB sphere and a 66 g steel sphere. (a) Acceleration of the magnet in the lower half of each of the 39 drops (light), calibrated on its steel sphere, with the mean and standard error of each session block; dashed: g less air drag. (b) Parts of the lower-half acceleration common to both orientations (even) and reversing with orientation (odd); grey: individual days; diamond: mean and standard error

5.2 Pendulum: magnets and steel sphere

5.2.1 Method

The 66 g steel sphere of the free-fall drops and two N45 NdFeB block magnets, $50.8 \times 25.4 \times 9.5\,mm$ each and about 188 g together (one of them weighs 94 g, Sec. 5.4; the 184 g of the first published version was inferred), stacked flat, were hung in turn from the same nylon twine, 3 g in mass and about 2 m long, and released 70 cm from the vertical, an amplitude of about 21°. Each run was filmed at 60 frames per second for 60 s (IMG_8754, steel sphere; IMG_8755, magnets). The bob was located in each frame by subtracting a background renewed every second, which follows a shift of the camera of about 2 pixels near the end of the steel record, and the time of each turning point, at both ends of the swing, was refined with a parabola through the neighbouring frames; the period is the slope of the turning times against the swing count. Both records hold the same number of turning points after the release, 21 at the near end and 20 at the far end, and all of them are used. The magnets turned about the rope during the swings, which leaves their centre in place.

5.2.2 Results

Over the same 20 swings, the steel sphere swings with a period of 2.8301 ± 0.0005 s and the magnets with 2.8528 ± 0.0009 s: the period of the magnets is 0.80 ± 0.03 % longer, and the crossings of the middle of the swing give 0.82 %. The magnets reach each turning point later than the sphere by a time that grows by 0.023 s per swing, to 0.56 s at the last near turning point (Fig. 10a); this lag stays below half a swing, the resolution of a count of the swings, and both records give the same count. The period of the steel sphere at zero amplitude, with the mass of the rope, corresponds

to a length of 1.98 m from the pivot to its centre. Three effects of the apparatus shift the two periods differently (Table 4): the mass of the rope, a larger share of the lighter bob, shortens the period of the steel sphere more; the swing of the magnets decays more slowly, from about 20.5° to 14.7° against 12.0° for the sphere, as measured from the height of the bob in the image, which keeps their amplitude, and so their period, slightly higher; and the centre of the flat stack of magnets hangs 3.1 mm higher than the centre of the sphere. After these the period of the magnets is 0.56 ± 0.06 % longer. The extra stretch of the twine under the heavier bob, estimated from the modulus of nylon, removes a further 0.02 to 0.09 %. The difference that remains is 0.47 to 0.53 % (±0.06 %). For an ideal point pendulum, $m_g/m_i = (L_{mag}/L_{steel})(T_{steel}/T_{mag})^2$: with equal effective lengths and unchanged non-gravitational torques, the remaining difference would correspond to m_g/m_i of 0.989 to 0.991 (±0.001) for the magnets, a conditional equivalent and not a measured mass ratio. With an unchanged mass ratio, the same difference would instead correspond to an effective length of the magnets' pendulum longer by 18.5 to 21.2 mm, so the two readings cannot be separated without the effective lengths known to a few millimetres; these effects were computed with the 184 g first inferred for the magnets, and with 188 g each changes by less than 0.01 percentage point, the difference that remains being 0.46 to 0.53 % and the longer effective length 18.3 to 21.1 mm; the 1.98 m length is itself inferred from the steel period with the same model. The quoted ±0.03 % is the precision of the period within each recording, and its near-end and far-end estimates come from the same recording and may share systematic errors; with one recording per bob, the reproducibility between runs is not measured. The rope and centre corrections are calculated from the geometry, the decay correction is measured from the swing amplitudes, and the stretch is a sensitivity interval for nylon moduli of 0.5 to 2 GPa, not a confidence interval.

Table 4 Difference between the periods of the magnets and of the steel sphere on the same rope, and the effects of the apparatus. Values are rounded; each remaining row is computed before rounding; the rows of the rope and of the stretch use the 184 g first inferred for the magnets (see text)

	Period of the magnets longer by (%)
Measured	$+0.80 \pm 0.03$
Mass of the rope, 3 g on 66 g and on 184 g	-0.24
Slower decay of the swing of the magnets, measured	-0.09 ± 0.02
Centre of the magnets 3.1 mm higher	$+0.08 \pm 0.05$
Remaining	$+0.56 \pm 0.06$
Extra stretch of the nylon twine under 184 g, estimated	-0.02 to -0.09
Remaining with the stretch	+0.47 to +0.53 (±0.06)
Conditional equivalent m_g/m_i, equal effective lengths	0.989 to 0.991 (±0.001)

5.2.3 Status

Open. Reanalysis of the tracks gives a period difference of 0.80 ± 0.03 % between the two recorded configurations; under the stated apparatus corrections the residual difference is 0.47 to 0.53 %. In an ideal equal-effective-length comparison with unchanged non-gravitational torques, this would correspond to a gravitational-to-inertial mass

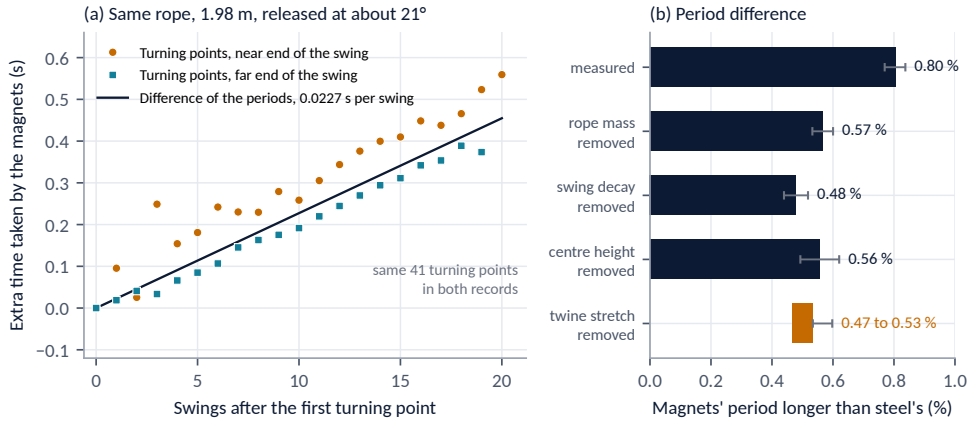

Fig. 10 Pendulum with the 66 g steel sphere (IMG_8754) and the pair of NdFeB blocks (IMG_8755) on the same rope. (a) Extra time taken by the magnets to reach each turning point, counted from the first turning point at the same end of the swing; the line is the difference of the two periods. (b) Difference between the two periods as measured and after each effect of the apparatus in Table 4; the last bar spans the estimated stretch of the nylon twine

ratio near 0.990 for the magnets. The present measurements do not isolate that interpretation from suspension, geometry and magnetic effects: bobs of different mass and shape change the loading, the attachment, the damping and the rotational coupling, and torsional and magnetic torques on the turning magnets are not excluded. Matched holders and shapes, measured loaded lengths, controlled swing amplitudes, alternating repeated runs, a non-magnetic mass-matched bob and field checks would test whether the difference persists under better-matched conditions.

5.3 Magnet floating on water

5.3.1 Method

The two N45 block magnets of Sec. 5.2, or one of them (94 g), were laid flat on a polystyrene float 15 cm wide and of 23 g, in a clear plastic container 60 cm long. The float was released in the middle of the container and filmed from the side through the near wall at 60 frames per second, and located in each frame by subtracting the background. Free to turn, the float first turned like a compass until the length of the magnets lay along the field of the Earth. The blocks are magnetized through their 9.5 mm thickness [30], so that their magnetization, laid flat, is vertical and not along that 50.8 mm length, as the first published version stated. Three sessions were made:

- **Afternoon, 16 h.** Container raised on plastic boxes in a closed room and standing in sunlight; two blocks, in both orientations on the float (IMG_8733, and IMG_8735 with the magnets turned over). Distances use the scale of the far wall, 15.4 pixels per cm, and are upper bounds, because the float is nearer the camera.
- **Night, 22 h.** Same container and place, without sunlight; one block and two blocks, each in both orientations, labelled N and S in the records (IMG_8745 to IMG_8748).

Distances use the width of the float, 16.5 pixels per cm. The float without the magnets was then placed in the same container.

- **Basement, plastic support.** Container on a plastic storage box, with no steel under it, its length running east–west; one block (IMG_8765) and two blocks (IMG_8766), each released in the middle of the container. The float was located by an edge of its image in a band at the waterline, and distances use the length of the container, 16.5 pixels per cm.

Each drift was fitted with a constant force from a free onset time, opposed by a water drag linear in the speed, giving the initial acceleration a_0 as an output of that assumed model; the steady speed is the slope of the later part of the track, before the wall. IMG_8766, which slowed down from the end of its turn, is described instead by its initial speed and the time constant of its slowing. A phone magnetometer moved along the length of the container in 10 cm steps, on a plank laid on the supporting box, read the field at that level.

5.3.2 Results

The principal runs are those on the plastic support, with no steel under the container (Fig. 12b). One block drifted west from the middle of the container, reaching 2.2 mm/s within about 5 s and keeping that speed for about 50 s, 14.7 cm in 71 s (IMG_8765). Two blocks first turned like a compass for about 15 s and then drifted east from the same starting point, starting at 2.9 mm/s and slowing to 1.0 mm/s with a time constant of 73 s, 14.1 cm in 80 s (IMG_8766). Without the magnets, the float did not move.

In the afternoon the float drifted toward magnetic north in both runs (Fig. 11); at night it drifted toward magnetic south in all four runs, with one block or two and whichever way the magnets were placed (Fig. 12a). Table 5 gives the fits. At night the steady speed was 2.4 to 3.2 mm/s and the float covered 13 to 18 cm in 51 to 111 s; one block and two blocks drifted alike. The float without the magnets did not move.

The magnetometer read a total field of 53.1 to 53.8 μT along the container, close to the 53.3 μT of the geomagnetic reference model at the site [19], with a horizontal component that varied by up to 3.5 μT over 50 cm; part of this variation may come from small tilts of the phone.

Table 5 Fits of the floating-magnet drifts, all with the same script: initial acceleration a_0 for a constant force opposed by linear water drag, and steady speed before the wall. Afternoon distances use the scale of the far wall and are upper bounds. IMG_8766 slowed down after its turn and is given by its speed at the start and at the end

Run	Magnets	Direction	a_0 (mm/s^2)	Speed (mm/s)	Travel (cm)
IMG_8733, 16 h	two	north	0.47	5.2	20
IMG_8735, 16 h	two, turned over	north	2.07	6.9	19
IMG_8745, 22 h	two, S	south	0.19	2.8	12.6
IMG_8746, 22 h	two, N	south	0.07	2.4	15.7
IMG_8747, 22 h	one, S	south	0.21	3.2	18.0
IMG_8748, 22 h	one, N	south	0.25	2.5	16.2
IMG_8765, plastic	one	west	2.07	2.2	14.7
IMG_8766, plastic	two	east	–	2.9 to 1.0	14.1

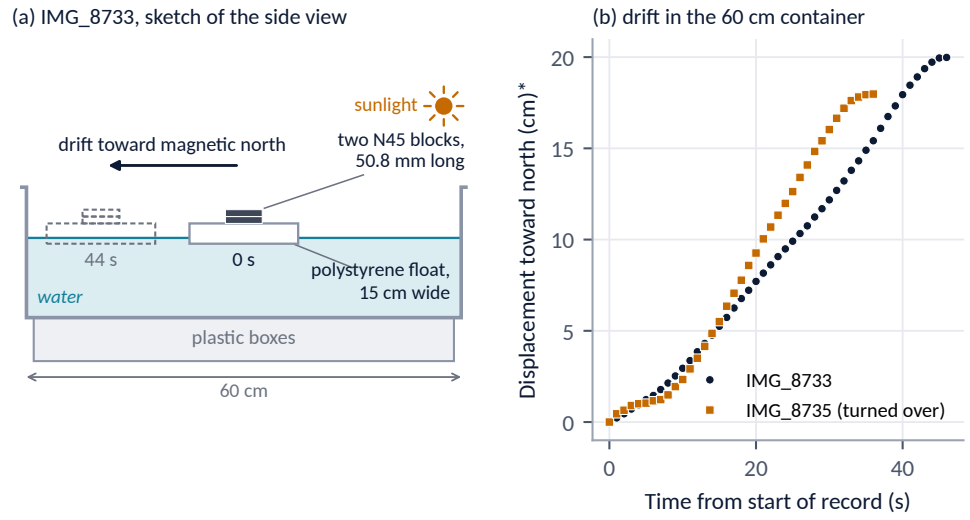

Fig. 11 Magnet floating in a 60 cm container on plastic boxes, in the afternoon. (a) Sketch of the side view (IMG_8733) at the start of the record and after 44 s; heights are not to scale. (b) Displacement toward magnetic north for both orientations of the magnets; *distances use the scale of the far wall and are upper bounds

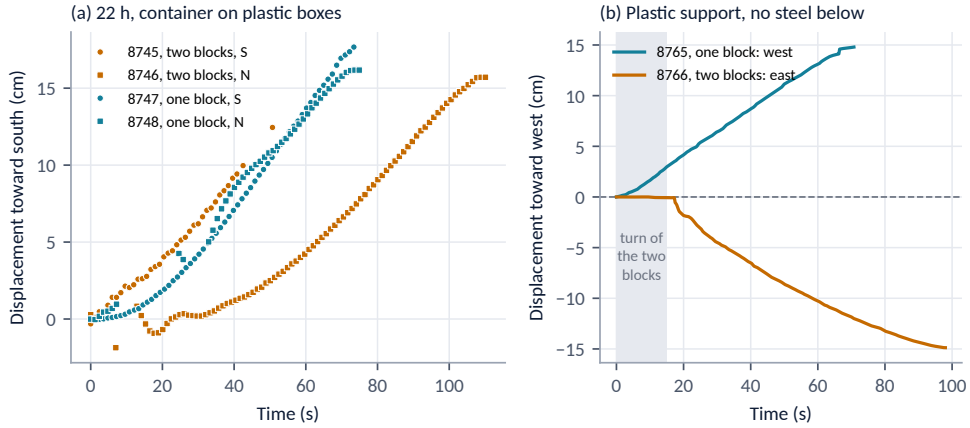

Fig. 12 Magnet floating on water. (a) Night runs in the same container and place, with one block or two in both orientations: displacement toward magnetic south. (b) Plastic support in the basement, with no steel under the container: displacement toward the west from the middle of the container, one block (IMG_8765) and two blocks (IMG_8766), which first turned during the shaded interval

5.3.3 Status

Open; no new force is established. On the plastic support, with no steel under the container, the float drifts, one block toward the west and two blocks toward the east from the same starting point, and the float without the magnets does not move; the cause of this drift is not identified, and ordinary magnetic and environmental interactions, such as variations of the field, residual ferrous material and surface currents, are not excluded; the drift of the two blocks slowed down after their turn. The bare float is lighter by 94 to 188 g and so differs in loading, immersion and drag; it is not a matched control. The initial accelerations of Table 5 are outputs of the assumed constant-force and linear-drag model, and the afternoon distances are upper bounds. The afternoon runs stood in sunlight, which can drive surface currents.

5.4 Weight of a magnet with either face up

5.4.1 Method

After the first publication of this article, one of the N45 block magnets of Sec. 5.2, magnetized through its 9.5 mm thickness [30], was weighed on a pocket jewellery scale reading to 0.001 g, with each of its two large faces up in turn, 20 times in all. The block lay flat on a cardboard box 9 cm high standing on the pan, with which the scale was tared, so that its magnetization was vertical and was reversed when the block was turned over. As a check of the scale, the block was also held at that height above the pan without touching it.

5.4.2 Results

In the recorded pair of weighings the scale read 93.925 g with one face up and 94.056 g with the other, a difference of 0.131 g, 0.14 % of the weight of the block. Over the 20 weighings the difference was 0.1 ± 0.03 g, consistently. With the block held above the pan, the scale read zero.

5.4.3 Status

Open; an apparent anomaly under investigation, and no new force is established. One pair of readings is recorded (Sec. 8.5); the other readings are not part of the released records. The interpretation of the difference is under investigation and is not given here. The check with the block held above the pan shows that the magnet does not act on the weighing mechanism; it does not test a force acting on the magnet itself, which the scale weighs with it. Turning the block over reverses its magnetic moment, about $13\,A\,m^2$ along the vertical, and with it the force that a non-uniform ambient field exerts on it: a vertical field changing by 40 to 50 μT per metre at the block, from steel or magnetized parts of the scale, of the support or of the building, would give the measured difference, and is not excluded by this check. In the record the box extends beyond the scale, and one end of the block lies about 1 cm beyond its edge, so that the load is off the centre of the pan; an effect of this off-centre load, or of a contact of the box with the body of the scale, is not excluded by the record. The uniform part of the field of the Earth exerts no net force on the block.

5.5 Spinning disc on a beam balance

5.5.1 Method

A 13 g polycarbonate disc (a compact disc of radius 60 mm) was spun about a vertical axis by a small DC motor, counterclockwise as seen from above. The motor and disc stood on one pan of an Ohaus two-pan beam balance, and the supply voltage and current were recorded. The disc speed was read from the acoustic tone of the rotor and the beam position from video of the pointer against its scale.

Four runs are reported: IMG_8693 (2062 to 2751 rpm), IMG_8694 (1413 to 2692 rpm), IMG_8695 (1785 to 2591 rpm) and IMG_8699, in which the supply was stepped from 2.5 to 4.5 V (1904 to 3056 rpm). IMG_8699 includes its own calibration: a 2.50 g coin dropped onto the pan in the same recording gives 11.98 g per window width of the pointer scale (±3 %), and this calibration is applied to all runs. Runs IMG_8693 and IMG_8694 have no calibration in frame; their readings are transferred with a scale known to ±25 % and may start from a different rest position. The beam stops limit the measurable lightening to 2.49 g (24.4 mN) from the pointer's rest position.

Table 6 Apparent change of weight Δm of the spinning-disc assembly (+ = lighter) and the equivalent axial force $F = \Delta m\, g$. Uncertainties include the calibration of each run. [a]Provisional conversion: transferred scale (±25 %), rest position and stop not known. [b]Within its uncertainty of the 2.49 g stop; whether the pointer was free is not established

Run	n (rpm)	Δm (g)	F (mN)
IMG_8694	1413	$+1.34 \pm 0.35$	$+13.2 \pm 3.4$
IMG_8695	1785	$+1.17 \pm 0.15$	$+11.5 \pm 1.5$
IMG_8699	1904	$+1.22 \pm 0.10$	$+11.9 \pm 1.0$
IMG_8693	2062	-0.70 ± 0.35	-6.9 ± 3.4
IMG_8695	2140	-1.23 ± 0.15	-12.1 ± 1.5
IMG_8694	2180	-0.95 ± 0.35	-9.3 ± 3.4
IMG_8695	2369	0.16 ± 0.19	1.6 ± 1.9
IMG_8699	2372	0.39 ± 0.12	3.9 ± 1.2
IMG_8694	2444	1.66 ± 0.64	16.2 ± 6.2
IMG_8695	2470	2.25 ± 0.35	22.1 ± 3.4
IMG_8693	2503	1.50 ± 0.40	14.7 ± 3.9
IMG_8695	2591	2.59 ± 0.28^{b}	25.4 ± 2.8^{b}
IMG_8694	2692	3.20 ± 0.82^{a}	31.4 ± 8.0^{a}
IMG_8693	2751	3.48 ± 0.88^{a}	34.2 ± 8.7^{a}
IMG_8699	3056	≥ 2.32	≥ 22.8 (at beam stop)

5.5.2 Results

Table 6 and Fig. 13 give all readings. The balance indicates speed-dependent load changes: sign changes below about 2400 rpm and apparent lightening above, in all four runs, and the calibrated run IMG_8699 reached the beam stop, at 2.32 g or more, at 3056 rpm. Some observations are limited by the stops or by an uncertain transferred calibration. The IMG_8695 reading at 2591 rpm lies within its uncertainty of the 2.49 g stop, and whether the pointer was free cannot be established from the record; the

IMG_8693 and IMG_8694 readings at 2692 and 2751 rpm carry the ±25 % transfer scale, and because those runs may start from a different rest position, their stop is not known. These three readings are provisional conversions, not established point values, and no maximum lightening is established.

As a descriptive fit only, the four readings of runs IMG_8693 to IMG_8695 between 2369 and 2503 rpm, clear of the stop and above the change of sign, follow

$$\Delta m = A \left[\left(\frac{n}{n_0} \right)^{5/2} - 1 \right], \qquad n \geq n_0 \tag{100}$$

with A and n_0 both fitted, the threshold n_0 being the speed at which the fitted curve crosses zero. These readings were selected after inspecting the data. The 2444 and 2503 rpm readings come from IMG_8694 and IMG_8693, whose scale is transferred and whose rest position is not known; both lie below later readings of the same runs, so the pointer was not at a stop there, and the transferred scale is in their uncertainties. A fit weighted by the uncertainties gives $A = 12.9 \pm 4.5$ g and $n_0 = 2353 \pm 28$ rpm, with $\chi^2 = 6.1$ for 2 degrees of freedom; the parameter uncertainties are scaled by $\sqrt{\chi^2/2}$, which does not correct clipping, an unknown zero or a shared calibration bias, and the uncertainty of the speeds, read from the acoustic tone, is not included. The exponent 5/2 was fixed; the measured power–speed exponent of the drive is 2.42. The readings do not determine it: a straight line through the same four points fits equally well ($\chi^2 = 5.9$), crossing zero at 2354 rpm. The exponent and the threshold are therefore not uniquely identified, and n_0 is a feature of the fitted curve, not an established physical threshold. As a sensitivity illustration, adding the 2591 rpm reading gives $A = 9.6 \pm 2.4$ g and $n_0 = 2339 \pm 34$ rpm, and adding the three uncertain readings gives $A = 8.4 \pm 1.7$ g and $n_0 = 2328 \pm 33$ rpm ($\chi^2 = 10.5$ for 5 degrees of freedom). The calibrated run IMG_8699 was not used: at 2372 rpm the fit gives 0.27 g and the run measured 0.39 ± 0.12 g; at 3056 rpm the run reached the stop at 2.32 g, a lower bound that does not test the extrapolation of the fit.

At 2591 rpm, from the reading near the stop, which is not an established point value, the supply delivered 0.667 W (3.73 V, 0.179 A), and the apparent force per unit input power was about 38 N/kW. This is an apparent load per input power, not an efficiency: it can exceed the 3.3 μN/kW of a beam of light carrying the same power when momentum is exchanged with the air or the supports.

Below about 2400 rpm the readings change sign: the pan was lighter by 1.2 to 1.3 g between 1413 and 1904 rpm and heavier by 0.7 to 1.2 g between 2062 and 2180 rpm, each seen in three runs. In repeat runs at 0.86 W input, both directions of rotation made the pan lighter, counterclockwise more than clockwise.

5.5.3 Status

Open. The apparent lightening above about 2400 rpm recurs in four runs, but its cause has not been separated from the apparatus. At 2591 rpm the rim of the disc moves at 16.3 m/s and the disc moves air above the pan; vibration of the beam near its resonances and forces from the supply leads act at the same scale. The sign changes below about 2400 rpm, and the lightening in both directions of rotation, are not expected of a force along the spin axis. A net upward force on the weighed

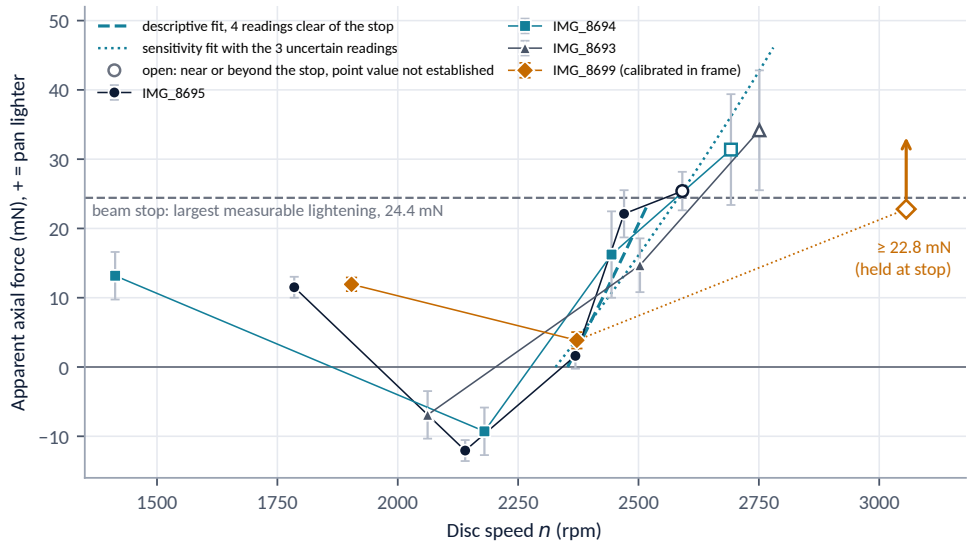

Fig. 13 Apparent axial force on the spinning-disc assembly against disc speed (+ = pan lighter; 13 g disc, counterclockwise), all readings of Table 6, joined within each run. Dashed: the descriptive fit (100) to the four readings of runs IMG_8693 to IMG_8695 clear of the stop; dotted: the sensitivity fit with the three uncertain readings, drawn open. Diamonds: run IMG_8699, calibrated in frame; its 3056 rpm reading is held at the beam stop and is a lower bound

assembly requires compensating momentum in the external air, fields or supports. A cover fixed to the pan around the disc would keep much of the moving air inside the weighed system, though it also changes the airflow and leaves pressure, vibration and lead forces. Operation at reduced pressure, a non-rotating vibration source of matched amplitude, and nulling the beam with its rider instead of reading the pointer against the stops are further checks.

5.6 Liquid-gallium vortex

An earlier run drove liquid gallium in a cell on a balance with a magnetohydrodynamic (MHD) drive at a current of about 100 A. The rotation speed of the gallium was not measured, and magnets placed above and below the cell cancelled the magnetic field at mid-depth, so the metal was not driven as intended. The balance reading, 2.6 ± 3.7 g, is consistent with zero.

Status. Inconclusive: the run constrains neither the presence nor the size of an effect. A comparison with the disc of Sec. 5.5 requires a run with a single-sided field, a measured rotation speed and stepped input power.

6 Conclusion

In this proposal, Finite Theory reproduces the first-order gravitational time dilation with the adopted $\lambda_g = c^2/G$; with the speed of light postulated to vary as the square of the time rate, and with its adopted orbital law, it reproduces the bending and the delay

of light and, to leading order, the perihelion shifts of the planets (Sec. 2), coinciding in these tests with General Relativity to first order; and it describes galactic rotation curves by a fit to each galaxy. Its cosmological inferences (Sec. 4) are conjectures, conditional on the assumptions stated there.

The bench experiments of Sec. 5 are summarized in Table 2. Under the adopted steel-reference calibration, the fitted lower-half acceleration of the magnet in the free-fall drops is about 21 % below the reference value, which unresolved calibration-transfer effects prevent identifying as a physical anomaly. The two pendulum configurations differ in period by 0.80 %, and by 0.47 to 0.53 % after estimated corrections, a difference whose reading as a mass ratio is conditional on the effective-length and restoring-force model. A floating magnet drifts in a direction that changes between runs, also on a plastic support with no steel under the container, where one block and two blocks drifted in opposite directions from the same starting point; its cause is not identified, and no new force is established. A block magnet weighed with either face up differs by 0.1 g between its faces, an apparent anomaly under investigation, for which a non-uniform ambient field is not excluded. The spinning disc gives speed-dependent load changes whose cause has not been separated from aerodynamic and mechanical effects, and the gallium vortex run was inconclusive. None of these measurements presently validates the proposed mechanism; the theory motivated these exploratory tests, and their present outcomes do not identify its mechanism.

Table 7 gives the status of each problem treated in this paper, in Finite Theory and in General Relativity.

Unresolved problems remain, and the model is offered as a conjecture for further theoretical and experimental investigation. An interferometer experiment proposed in an earlier version for the International Space Station is archived with the records [9], together with its open steps.

7 Acknowledgments

This article was still a pure theoretical facet in the year 2005 and was fostered into serious labor after Dr. Griest considered it worth pursuing and set important requirements. Many thanks to him.

Furthermore my father, Mr. Bouchard MSc. Nuclear Physics, brought considerable help in asserting the mechanical part of my equations. He also introduced me to the astrophysical society for advanced research.

The same goes directly and indirectly for the online scientific community, where we can find Cosmoquest.org, InternationalSkeptics.com, NaturalPhilosophy.org, APEC (now AltSci.net), and the League of Extraordinary Inventors, in order to have the opportunity to break the ice and debate theories that are against the mainstream.

Also thanks to Dimtcho Dimov for some help solving equations, Evan Adams for reviewing related experiments and Nicholas Percival for helping edit it and for assistance with the ISS National Lab.

Table 7 Status of each problem treated in this paper, in Finite Theory and in General Relativity: resolved (reproduced), unresolved (in conflict with the measurements or not accounted for), open (not yet compared with the measurements), fitted (parameters adjusted to each data set), conjecture (conditional on assumptions not tested here) or not addressed. The solar-system tests of General Relativity are reviewed in [34]

Problem	Finite Theory	General Relativity
Clock rates: time dilation, redshift, GPS (Secs. 2.8 to 2.10)	Resolved to first order, with the adopted $\lambda_g = c^2/G$	Resolved
Bending of light (Sec. 2.6)	Resolved with the postulated second factor of the light speed; a consistency, not an independent prediction; the same as General Relativity to first order	Resolved
Perihelion shift (Sec. 2.7)	Resolved to leading order, with the adopted orbital law, consistent to that order with the clock law and the light speed	Resolved
Delay of light (Sec. 2.6)	Resolved with the same postulate ($\gamma = 1$ to first order)	Resolved ($\gamma = 1$)
Earth–Moon light time (Sec. 4.1.1)	Open: 0.24 m from a flat-propagation baseline, not compared with ranging data	Resolved in lunar laser ranging
Spread of the measured G (Sec. 2.11)	Unresolved: a latitude dependence matches its size but not all the measurements	Unresolved: no cause identified
Earth-tide residual (Sec. 4.2)	Conjecture: compatible with an æther wind; a timing offset not excluded	Not addressed
Flyby anomaly (Sec. 4.2)	Conjecture: compatible with an æther wind	Unresolved
Galactic rotation curves (Sec. 4.3.1)	Fitted: three parameters per curve, without dark matter	Fitted with dark matter, not detected directly [1]
Accelerated expansion (Sec. 4.3.2)	Conjecture: the universal core restates the assumptions	Fitted with dark energy, of unknown nature
Nuclear forces (Sec. 3)	Conjecture: not evaluated against nuclear data	Not addressed
Bench experiments (Sec. 5, Table 2)	Open: no anomalous force established	Conventional forces on the apparatus; no anomalous force predicted

8 Declarations

8.1 Ethical approval

Not applicable.

8.2 Competing interests

The author is the founder and CEO of Fornux, which develops technologies based on the work reported here. The author declares no other competing interests.

8.3 Authors' contributions

P. Bouchard wrote the entire theory and manuscript from scratch.

8.4 Funding

Not applicable.

8.5 Availability of data and materials

The data, materials and the code used to analyze the data that support the findings of this study are openly available on GitHub (see [6] and [7]). The dataset includes 497 galactic rotation curves of 486 galaxies and microgal measurements of the Earth's tides. Users are free to download and use the data for non-commercial purposes, with proper attribution to the authors. The earlier free-fall prediction, withdrawn from this paper, and the per-session free-fall summary are available at [8] and [11]; the records of the bench experiments of Sec. 5 (the 40 tracked drops, the pendulum and floating-magnet tracks, the phone magnetometer records and the spinning-disc readings) and the scripts that reproduce Tables 3 to 6, the fits of Sec. 5.5.2 and Figs. 9, 10, 12 and 13 are released with run instructions in [9], the file bench-v1.2.zip on the master branch of the repository (SHA-256 `80eff6a65b79fca2c9b25be52dc29483 3863594642fb07a5bbe84fc265d132c2`), with the survey and Milky Way fits and Figs. 7 and 8 of Sec. 4.3.1 and the archived interferometer proposal. The record of the weighing test of Sec. 5.4 is not part of it; it is available from the author on request (Magnet-Scaled.mp4, SHA-256 `60033b3e02dadcd7f0916807266d9ffc a21eef1443d8101beac36a624caa19b0`). The video records, identified there by their SHA-256 hashes, and the videos of the free-fall, spinning-disc and gallium-vortex runs are available from the author on request. The source code of the Finite Theory simulator is openly available under the GNU General Public License [10].

8.6 Corrections to the version first published

In the version of this article first published in this journal, the distant-observer speed of light (43) carried the first power of the time rate, and the ray law (45) added the Newtonian acceleration to the refraction of the index. That law reproduced the bending of light but gave half of its measured delay, which was reported as an open problem. In this version the speed of light carries the square of the time rate: the second factor is attributed to the energy density of the superimposed potential, with which matter scales, and the Newtonian term of the ray law is removed. The bending and the delay of light are then both reproduced to first order, where the model coincides with General Relativity. The abstract, Table 1, Secs. 2.2.2, 2.6, 2.7 and 4.1, the conclusion and Table 7 are changed accordingly. A weighing test made after the first publication is added as Sec. 5.4, with its entries in the abstract, Table 2 and the conclusion, and the direction of magnetization of the block magnets (Sec. 5.3.1) and their mass, 94 g each as weighed in place of the 92 g first inferred (Secs. 5.2 and 5.3), are corrected. The clock rates, the orbital law, the rotation-curve fits, the other bench results and the released records were unchanged by that correction.

A second correction changes the clock law at second order. In the version first published and in the first correction, the clock rate was the ratio $\lambda/(\lambda+S)$. Read with the light speed (43) as a line element, that ratio gives the post-Newtonian parameter $\beta = 3/2$: a body on a path of extremal proper time would advance its perihelion by five sixths of the observed value, so that the adopted orbital law of Sec. 2.7, which gives the whole, did not agree with the clock law and the light speed. The clock rate is now (40), with an adopted second-order term for which $\beta = 1$, and the adopted orbital law agrees with that line element to first order. The first-order relations and their numerical results are unchanged. The rotation-curve formula (91), which uses the clock rate where S/λ is not small, changes with it: the 497 curves and the Milky Way are fitted again (mean standard deviation 7949 m/s in place of 8031 m/s; Milky Way 7.6 km/s in place of 6.7 km/s, with $\lambda_g = 4.1 \times 10^{21}$ in place of $3.5 \times 10^{21}\, kg\, m^{-1}$), Figs. 7 and 8 are redrawn, and release bench-v1.2 replaces bench-v1.1, from which it differs in the galaxy fits only. Hypothesis 5 is added: it reads the adopted form in terms of energy and was formulated after it. The former Definition 4, of the kinetic energy, is merged into Hypothesis 2, so that the former Definition 5 is now Definition 4, and Hypothesis 3 is restated as a force, without its clauses on time dilation and temperature. Definition 4, Table 1, Secs. 2.2.1, 2.5.3, 2.5.4, 2.6, 2.7, 2.8.2, 2.9, 3.1, 4.1 and 4.3.1, Table 7 and the data statement are changed accordingly. The interaction energy of Sec. 3 keeps the ratio, and the bench results are unchanged.

References

[1] J. Aalbers et al. Dark matter search results from 4.2 tonne-years of exposure of the LUX-ZEPLIN (LZ) experiment. *Phys. Rev. Lett.*, 135:011802, 2025. doi: 10.1103/4dyc-z8zf.

[2] N. Ashby. Relativity and the Global Positioning System. *Physics Today*, 55(5): 41–47, 2002. doi: 10.1063/1.1485583.

[3] J. Bailey, K. Borer, F. Combley, H. Drumm, F. Krienen, F. Lange, E. Picasso, W. von Ruden, F.J.M. Farley, J.H. Field, W. Flegel, and P.M. Hattersley. Measurements of relativistic time dilatation for positive and negative muons in a circular orbit. *Nature*, 268:301–305, 1977.

[4] W. Bertozzi. Speed and kinetic energy of relativistic electrons. *American Journal of Physics*, 32:551–555, 1964.

[5] J. Bland-Hawthorn and O. Gerhard. The galaxy in context: Structural, kinematic and integrated properties. *Annu. Rev. Astron. Astrophys.*, 54:529–596, 2016. doi: 10.1146/annurev-astro-081915-023441.

[6] P. Bouchard. Finite theory's galactic rotation curve formula applied to various galaxies, 2022. URL https://github.com/philippeb8/grc.

[7] P. Bouchard. Residual of the earth's tides is showing consistent "æther wind", 2022. URL https://github.com/philippeb8/microgal.

[8] P. Bouchard. Finite theory – theory of freefall experiment, 2025. URL https://static.fornux.com/files/freefall/Finite_Theory-FreeFall-Theory.pdf.

[9] P. Bouchard. Finite theory bench experiments: records and analysis scripts, release bench-v1.2, 2026. URL https://github.com/philippeb8/finite-theory/blob/master/bench-v1.2.zip.

[10] P. Bouchard. ftsim – N-body simulator under Finite Theory's time-dilation factor, 2026. URL https://github.com/philippeb8/finite-theory. C++17/Qt6 source code, GNU General Public License v3.

[11] P. Bouchard. Finite theory – freefall – statistics, 2026. URL https://static.fornux.com/files/freefall/Finite_Theory-FreeFall-Statistics.pdf.

[12] R.T. Cahill. Lunar laser-ranging detection of light-speed anisotropy and gravitational waves. *Progress in Physics*, 2:31–35, 2010.

[13] T.P. Cheng. *Relativity, Gravitation and Cosmology. A Basic Introduction.* UK: Oxford University Press, 2005.

[14] T.P. Cheng. *Einstein's Physics. Atoms, Quanta, and Relativity Derived, Explained, and Appraised*. UK: Oxford University Press, 2013.

[15] P. Delva et al. Gravitational redshift test using eccentric Galileo satellites. *Phys. Rev. Lett.*, 121:231101, 2018.

[16] R. H. Dicke. Gravitation without a principle of equivalence. *Rev. Mod. Phys.*, 29:363–376, 1957. doi: 10.1103/RevModPhys.29.363.

[17] S. Herrmann et al. Test of the gravitational redshift with Galileo satellites in an eccentric orbit. *Phys. Rev. Lett.*, 121:231102, 2018.

[18] R.A. Hutchin. The physics behind the NASA flyby anomaly. *Optics and Photonics Journal*, 12(3):31–51, 2022. doi: 10.4236/opj.2022.123003.

[19] IAGA Division V, Working Group V-MOD. International Geomagnetic Reference Field, 14th generation (IGRF-14), 2024. URL https://doi.org/10.5281/zenodo.14012302.

[20] F. Lelli, S. S. McGaugh, and J. M. Schombert. SPARC: Mass models for 175 disk galaxies with Spitzer photometry at 3.6 μm and accurate rotation curves. *The Astronomical Journal*, 152:157, 2016. doi: 10.3847/0004-6256/152/6/157.

[21] B. Mashhoon. Gravitoelectromagnetism: A brief review, 2008. URL https://arxiv.org/abs/gr-qc/0311030. arXiv:gr-qc/0311030.

[22] P.J. Mohr, D.B. Newell, B.N. Taylor, and E. Tiesinga. CODATA recommended values of the fundamental physical constants: 2022. *Rev. Mod. Phys.*, 97:025002, 2025.

[23] G. Pipino. Evidences for varying speed of light with time. *Journal of High Energy Physics, Gravitation and Cosmology*, 5:395–411, 2019.

[24] R.V. Pound and J.L. Snider. Effect of gravity on nuclear resonance. *Phys. Rev. Lett.*, 13:539–540, 1964.

[25] M. Schirber. Gravitational constant's value still up in the air. *Physics*, 19:64, 2026. URL https://physics.aps.org/articles/v19/64.

[26] S. Schlamminger et al. Redetermination of the gravitational constant with the BIPM torsion balance at NIST. *Metrologia*, 63:025012, 2026.

[27] Y. Sofue. Atlas of surface mass density and mass-to-luminosity ratio in spiral galaxies, supplementary archive for sofue (2018), 2018. URL http://www.ioa.s.u-tokyo.ac.jp/~sofue/smd2018/.

[28] Y. Sofue. Rotation curve of the milky way and the dark matter density. *Galaxies*, 8:37, 2020. doi: 10.3390/galaxies8020037.

[29] N. Sorli, N. Gorjup, and R. Gorjup. Replacement of space-time with superfluid space and restoration of Newton's dynamic ether. *Reports in Advances of Physical Sciences*, 5, 2023.

[30] SuperMagnetMan. Rect2008 – rectangle magnet – 50.80mm long x 25.40mm wide x 9.52mm th – n45 – black epoxy coated, 2026. URL https://supermagnetman.com/products/rect2008. Product sheet; direction of magnetism: through thickness.

[31] J. P. Turneaure, C. M. Will, B. F. Farrell, E. M. Mattison, and R. F. C. Vessot. Test of the principle of equivalence by a null gravitational red-shift experiment. *Phys. Rev. D*, 27:1705, 1983. doi: 10.1103/PhysRevD.27.1705.

[32] R.F.C. Vessot, M.W. Levine, E.M. Mattison, E.L. Blomberg, T.E. Hoffman, G.U. Nystrom, B.F. Farrel, R. Decher, P.B. Eby, C.R. Baugher, J.W. Watts, D.L. Teuber, and F.D. Wills. Test of relativistic gravitation with a space-borne hydrogen maser. *Phys. Rev. Lett.*, 45:2081–2084, 1980.

[33] C.M. Will. *Theory and Experiment in Gravitational Physics*. UK: Cambridge University Press, 1993.

[34] C.M. Will. The confrontation between general relativity and experiment. *Living Rev. Relativ.*, 17:4, 2014. doi: 10.12942/lrr-2014-4.

[35] C. Xue, J.-P. Liu, Q. Li, J.-F. Wu, S.-Q. Yang, Q. Liu, C.-G. Shao, L.-C. Tu, Z.-K. Hu, and J. Luo. Precision measurement of the newtonian gravitational constant. *National Science Review*, 7(12):1803–1817, 2020.